This is a peer-reviewed, accepted author manuscript of the following research article:
Alaqabani, H, Hammad, A, Abosnwber, Y & Perrie, Y 2024, 'Novel microfluidic development of pH-responsive hybrid liposomes: *in vitro* and *in vivo* assessment for enhanced wound healing', *International Journal of Pharmaceutics*, vol. 667, no. Part A, 124884.
https://doi.org/10.1016/j.ijpharm.2024.124884

Novel Microfluidic Development of pH-Responsive Hybrid Liposomes: *In Vitro* and *In Vivo* Assessment for Enhanced Wound Healing

Hakam Alaqabani[a,b*], Alaa Hammad[b*], Yara Abosnwber[c], Yvonne Perrie[a]

[a] Strathclyde Institute of Pharmacy and Biomedical Sciences, University of Strathclyde, 161 Cathedral St, Glasgow G4 0RE, UK

[b] Faculty of Pharmacy, Al-Zaytoonah University of Jordan, Airport St, 11733 Amman, Jordan

[c] Faculty of Health School of Biomedical Sciences, Queensland University of Technology, 2 George St, Brisbane City QLD 4000, Australia

***Corresponding Authors:**

Alaa Hammad, Faculty of Pharmacy, Al-Zaytoonah University of Jordan, Airport St, 11733 Amman, Jordan

Email: alaa.hammad@zuj.edu.jo

Hakam Alaqabani, Strathclyde Institute of Pharmacy and Biomedical Sciences, University of Strathclyde, 161 Cathedral St, Glasgow G4 0RE, UK

Email: hakam.alaqabani@strath.ac.uk

#Electronic Supplementary Information (ESI) available: Optimization of Microfluidic Liposomes

Graphical Abstract

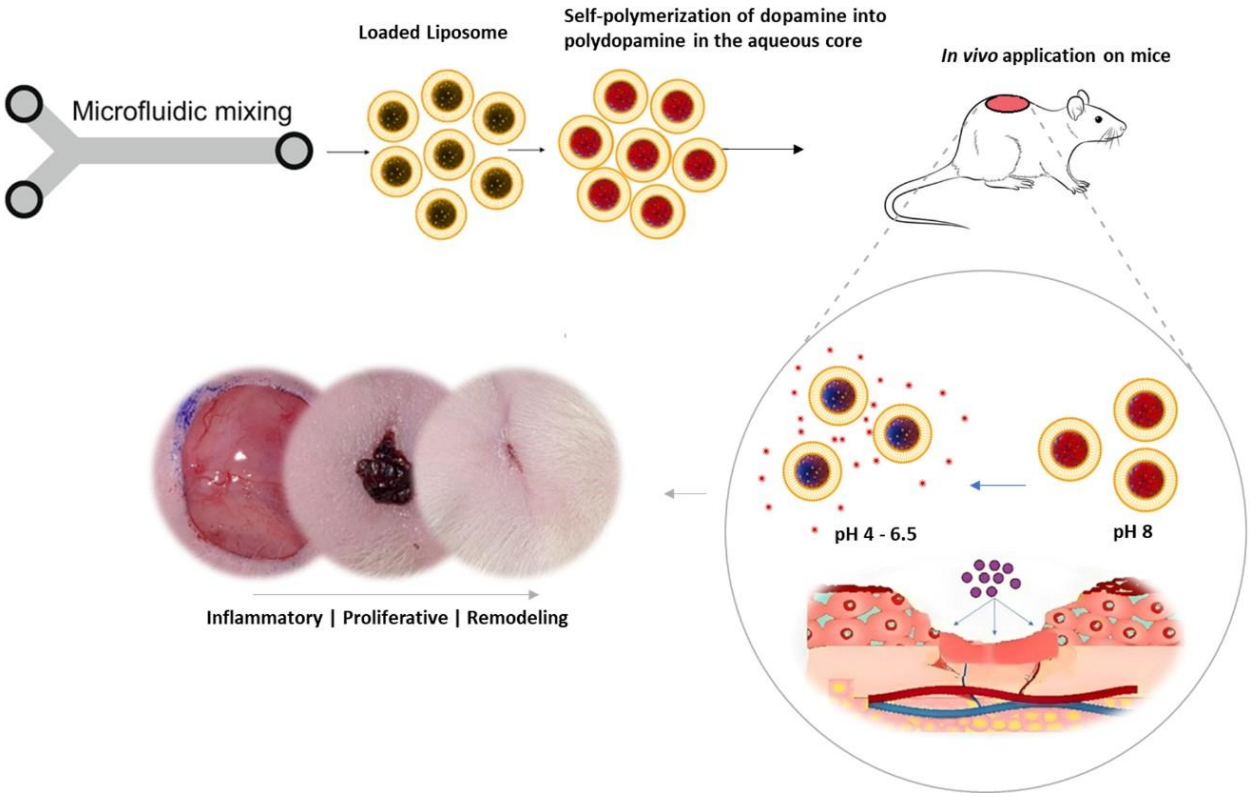

Abstract

Wound healing is a complex biological process crucial for tissue repair, especially in chronic wounds where healing is impaired. Liposomes have emerged as promising vehicles for delivering therapeutics to facilitate wound repair. Liposomes have been explored as effective carriers for therapeutic agents. However, traditional methods of liposome preparation face significant challenges, particularly in achieving consistent stability and precise control over drug encapsulation and release. This study addresses these challenges by pioneering the development of Hybrid Liposomes (HLPs) using microfluidic technology, which provides more controlled characteristics through precisely managed formulation parameters. Notably, the formation of Polydopamine (PDA) polymer within HLPs facilitates pH-responsive drug release, making them well-suited for acidic wound environments. Furthermore, surface modification with Folic Acid (FA) enhances cellular interaction with the HLPs. In vitro and in vivo studies demonstrate the efficacy of HLPs loaded with Hyaluronic Acid (HA) or Phenytoin (PHT) in promoting wound healing. Microfluidics optimizes the stability of HLPs over 90 days, underscoring their potential as a potent, antibiotic-free drug delivery system. In conclusion, this research advances the understanding of microfluidic optimization for HLPs, offering cutting-edge drug delivery systems. The transformative potential of targeted HLPs through microfluidics holds promise for revolutionizing wound healing and inspires optimism for effective therapeutic interventions.

Keywords: Microfluidics, Folic Acid, Targeted Drug Delivery, Hybrid Liposomes, Polydopamine, Nanoparticles.

1. Introduction

The restoration of tissue integrity is orchestrated through a complex interplay of cellular and molecular events in the process of wound healing(Lorenz and Longaker 2008). The effectiveness of this natural regenerative process relies on both the body's inherent reparative mechanisms and the applied supportive measures (Man and Hoskins 2020). Given the paramount importance of promoting the healing of wounds, the pursuit of new approaches to optimize therapeutic outcomes is ongoing. The management of chronic wounds presents formidable challenges and imposes significant costs on healthcare systems (Kolimi, Narala et al. 2022). Globally, a rising number of individuals suffer from chronic wounds annually, constituting a significant yet often overlooked health crisis. This increase is attributed to factors such as an ageing population, rising comorbidities, and lifestyle-related disorders such as diabetes and obesity. Chronic wounds not only impose a significant healthcare burden but also lead to substantial financial and psychological consequences (Simón 2016, Avishai, Yeghiazaryan et al. 2017, Sen 2021). Identifying high-risk individuals and implementing effective treatments is crucial in preventing the development of chronic wounds. The widespread impact of these health issues has sparked considerable interest in exploring innovative treatments with enhanced clinical efficacy.

Nanoparticles have sparked tremendous interest due to their potential uses in the area of wound healing (Naderi, Karponis et al. 2018, Bai, Han et al. 2020). These lipid-based nanocarriers possess a distinctive capacity to encapsulate and transport a diverse range of therapeutic substances, encompassing both traditional drugs and cutting-edge biologics (Al-Jamal and Kostarelos 2011). The versatility of nanoparticles holds great promise in the context of wound management. Additionally, the biodegradable and biocompatible properties of liposomes(Al-Jamal and Kostarelos 2011), along with their ability to moisturize dry wounds, render them a preferred choice for topical delivery systems, particularly in wound treatment(Bai, Han et al. 2020). Traditional liposome methods have potential but face formulation challenges and variations that can affect stability and quality. This study uses microfluidic technology to develop HLPs systems for topical applications. By more precisely controlling formulation parameters, to achieve more stable and effective formulations. Utilizing microfluidics enables the attainment of controlled physiochemical properties of nanoparticles, a crucial aspect of effective drug delivery (Ejeta 2021). The primary goal is to alter the composition and features of liposomes, ultimately improving their stability and enhancing their capability for targeted delivery with controlled release. Research findings, such as developing engineered polymeric nanoparticles for repairing damaged kidney podocytes, highlight the potential of advanced delivery systems for specific cell types and tissue repair (Colombo, Li et al. 2017). These specialized HLPs are utilized to support wound repair and promote better ability to heal quality. At the core of this innovative method lies the fusion of a lipid bilayer with a polymer matrix, a distinctive combination that strengthens liposomes, boost their stability, increase drug encapsulation efficiency (EE%), and provide precise control over drug release kinetics through the polymer containing the encapsulated drug. The incorporation of HLPs with a PDA polymer within the liposome core emerges as a promising strategy for controlled drug release. Microfluidic formulations ensure meticulous control over liposome characteristics, and the pH-responsive nature of PDA polymer selectively releases the drug in acidic pH (Zhang, Xu et al. 2020), leveraging its unique properties for controlled drug release and enhancing therapeutic efficacy in targeted regions.

This study explores the synthesis of HA and PHT HLPs with targeted FA for enhanced cellular interaction in wounds with thick or impaired barriers. The unique ability of FA to target skin cells and enhance skin penetration positions it as a promising tool for the development of innovative skin-targeted therapeutics. Folate receptors (FRs), abundant membrane-bound proteins in various skin cells, provide an opportunity for NPs

conjugated with FA to exploit this interaction. This triggers FR-mediated internalization, effectively enhancing drug delivery to the skin. FA's activation of macrophages, especially in inflammatory settings, further extends its potential utility in treating skin conditions characterized by inflammation (Frigerio, Bizzoni et al. 2019). Moreover, FA efficiently traverses the skin barrier by binding to receptors on the skin surface, including FRα or FRβ glycosylphosphatidylinositol (GPI)-anchored FRs and the reduced folate carrier (RFC). The initiation of a signaling cascade by FA enhances skin barrier permeability, promoting increased penetration and fostering heightened skin permeability(Knott, Mielke et al. 2007). The strategy aims to improve drug delivery in wound healing by combining FA targeting and PDA core-controlled release. The research repurposes PHT, known for gingival hyperplasia side effects (Farook, M Nizam et al. 2019), for its potential in wound healing within HLPs. Additionally, HA is incorporated for its tissue repair role(Yang, Song et al. 2020). In summary, this research introduces a novel approach to improve wound healing by creating functionalized HLPs with FA using microfluidic technology. These hybrid nanoparticles, which merge a lipid bilayer with a polymer matrix, offer enhanced stability, controlled drug release, and improved targeting through the inclusion of FA. Specifically designed for challenging wound scenarios, As this method seeks to elevate therapeutic results in wound management by emphasizing precise nanoparticle design and formulation.

2. Materials and Methods

2.1. Materials

Dopamine hydrochloride (Merck Life Science UK Limited), 1,2-distearoyl-sn-glycero-3-phosphocholine (DSPC) (18:0 PC) (Avanti Polar Lipids, USA), Ethanol 98% (Thermo Fisher Scientific, UK), HeLa and HEK-293 cells (American Type Culture Collection, ATCC, USA), Cholesterol (European Pharmacopoeia Reference Standard, Merck Life Science UK Limited), DMEM (Dulbecco's Modified Eagle Medium, Merck Life Science UK Limited), Fetal Bovine Serum (FBS, Fisher Scientific Limited, UK), Isopropanol (IPA, Fisher Scientific Limited, UK), Phosphate buffered saline tablets (PBS, Oxoid Ltd, Basingstoke, UK), Trypsin-EDTA Solution (American Type Culture Collection, ATCC, USA), Hyaluronic acid sodium salt from Streptococcus equi 8-15 KDa (Merck Life Science UK Limited), Phenytoin European Pharmacopoeia (EP) Reference Standard (Merck Life Science UK Limited), Folic acid meeting USP testing specifications (Merck Life Science UK Limited), NHS (N-Hydroxysuccinimide, Merck Life Science UK Limited), Dimethyl sulfoxide (DMSO, Merck Life Science UK Limited), EDC (1-Ethyl-3-(3-dimethyl aminopropyl)carbodiimide, Merck Life Science UK Limited), Acridine Orange hydrochloride hydrate≥98% (Merck Life Science UK Limited), DiIC18(5)-DS (1,1'-Dioctadecyl-3,3,3',3'-Tetramethylindodicarbocyanine-5,5'-Disulfonic Acid, Thermo Fisher Scientific UK), 1,2-distearoyl-sn-glycero-3-phosphoethanolamine-N-[PDP(polyethylene glycol)-2000] thiol **(**DSPE-PEG SH) (Biochempeg, USA), Carbazole, 95% (Thermo Fisher Scientific UK), Sulfuric acid ACS reagent, 98.0% (Merck Life Science UK Limited), Methanol, HPLC, ≥99.9% (Merck Life Science UK Limited), Human IL-1β ELISA Set II (BD OptEIA™, USA), Human TNF ELISA Set (BD OptEIA™, USA), White 96-Well Immuno Plates for ELISA (Thermo Fisher Scientific UK), Lipopolysaccharides from Escherichia coli O111:B4 (Merck Life Science UK Limited), 3,3′,5,5′-Tetramethylbenzidine, ≥99% (Merck Life Science UK Limited), and Hydrogen Peroxide 30% in water (Thermo Fisher Scientific UK), Cyclodextrin (CD) (Sigma-Aldrich, USA), 100 kD Biotech CE Dialysis Kits (MWCO: 100 kDa) (Spectrum™ Labs, USA), HEPES (4-(2-hydroxyethyl)-1-piperazineethanesulfonic acid) (Merck Life Science, UK). Furthermore, instrumental equipment and devices from various manufacturers were used, including IRSpirit. Fourier-transform infrared spectroscopy from Shimadzu, UK; Krosflo Research III TFF sourced from Spectrum Inc, Netherlands; Life Technologies EVOS FL Colour Imaging System AMF 4300 from Fisher Scientific Limited, UK; Malvern

Nano ZS acquired from Malvern Panalytical Ltd., The NanoSight Pro (NS Pro) Malvern Panalytical Ltd, Worcestershire, UK; Modified polyethersulfene (mPES) hollow fiber columns (750 kD MWCO) provided by Spectrum Inc, Netherlands; Multiskan SkyHigh Microplate Spectrophotometer from Fisher Scientific Limited, UK; NanoAssemblr® Benchtop Precision NanoSystems Inc, Canada; GloMax® Microplate Readers – Promega UK; CloudSpec UV-Vis Spectrophotometer Marama Labs; ImageJ software (NIH, Bethesda, MD). ChemDraw® software 22.0 (PerkinElmer Informatics Inc, USA) Additionally, *in vivo* studies involved a cohort of 28 female rats, necessitating the use of various surgical instruments. ChemDraw for drawing Chemical structures.

2.2. Methods

2.2.1. Synthesis and Characterization of DSPE-PEG-FA for Targeted Delivery

DSPE-PEG thiol is conjugated with FA through the EDC/NHS coupling reaction (Fischer 2010). FA activation commences by dissolving it in 1% NaOH (0.1M) methanol solution. The activation of FA occurs by mixing the FA, EDC, with NHS with a molar ratio of 1:10:5, then stirring gently for a few minutes and a 30-minute incubation in the dark at 25 °C to create the activated FA intermediate. This activated FA intermediate is highly reactive, making it susceptible to nucleophilic attack by thiol (-SH) groups found in DSPE-PEG thiol, forming covalent bonds. The activated FA solution is mixed with DSPE-PEG-SH in a molar ratio of one to one and stirred for 4 hours at room temperature. A stream of nitrogen gas is then used to remove the organic solvents. To facilitate the precipitation of DSPE-PEG-FA, which has limited solubility in water, 0.05% NaOH (0.1M) is added to the mixture. Afterwards, to remove excess EDC/NHS and unconjugated FA, the solution undergoes centrifugation at 12,000 rpm for 20 minutes. The supernatant is discarded, and the washing process is repeated five times to ensure that all impurities are removed completely. Finally, the pellet is collected and dried using a stream of nitrogen gas to enhance its stability. The Characterization of the DSPE-PEG- FA conjugate confirms the successful conjugation and evaluates the purity of the final product using UV-vis spectroscopy, FTIR spectroscopy and HPLC.

2.2.2. Controlled Microfluidics for Tailored Liposome Formulation

Liposomes were synthesized through microfluidic techniques using the NanoAssemblr® Benchtop system, provided by Precision Nanosystems. The procedure entailed dissolving lipids, including DSPC, cholesterol, and the modified DSPE-PEG- FA at a w/w ratio of 3:1:1 respectively (56:39:5 M ratio), in ethanol, with an initial concentration of 20 mg/mL. Adjustments were made to the NanoAssemblr® software to control essential production parameters, including the flow rate ratio (FRR), which determined the proportion between the aqueous and lipid phases, and the total flow rate (TFR), governing the collective injection speed of both phases through the microfluidic chip. Various FRRs (1:1, 2:1, 3:1) were explored, alongside TFRs ranging from 10 mL/min to 20 mL/min, with sufficient total volume to measure these parameters. These lipids were added into the left inlets on the microfluidic herringbone micromixer chip, while the aqueous phase, containing concentrations of DA (0.5 or 1 mg/mL), and (0.1-0.8mg/mL) of either PHT or HA which diluted immediately before injection into the microfluidic herringbone micromixer chip in (0.1 M, pH 7.4 ± 0.3), was introduced into the second inlet.

2.2.3. Solvent Removal and Liposome Purification

To remove residual ethanol solvents and unbound drugs from liposome samples, the Krosflo Research III TFF system equipped with a 750 kD mPES (modified polyethersulfone) column was used. The samples were

introduced into the column and underwent diafiltration, a process that involves replacing the solvent with fresh PBS buffer 7.4± 0.3. The filtration was conducted at a pressure of 1.6 psi (feed) and 1.1 psi (retentate), with a flow rate of 16 mL/min. This continuous purification process was performed over two cycles, and each millilitre of the sample was diluted by a factor of 12mL PBS buffer (0.1 M, pH 7.4 ± 0.3).

2.2.4. Sterilization of liposomes and Quantification of the lipid

Sterilization of the liposomes was accomplished using a sterile polyethersulfone (PES) 33 mm sterile syringe filter over 0.22 μm pore size (Millipore, Millex-GP). To evaluate the effect of sterilization on liposome yield, DiIC18-labeled liposomes were quantified using a protocol involving the incorporation of the DiIC18 fluorophore dye (Roces, Port et al. 2020), before microfluidics, incorporated into the lipid phase, as outlined by Forbes *et al*. (2019). DiIC18 was introduced to the lipid phase at 0.1% (w/w). Fluorescence intensity (FI) measurements were taken both before and after the purification process involving TFF, using optical configurations set at the wavelength (excitation: 520 nm, emission: 580-640 nm) with the GloMax® Microplate Readers- Promega. The liposome recovery was determined as a percentage of the initial amount, employing a calibration curve established with DiIC18-labeled liposomes produced by microfluidics.

2.2.5. Self-Polymerization of DA Within Liposomes to Form PDA Polymer

The polymerization of PDA was systematically achieved by the self-polymerization of DA in a higher pH environment within a liposome aqueous core. The addition of DA in the microfluidic setup occurred immediately before the injection step into the system to ensure that DA would initiate polymerization inside the liposome core after the formation of the liposome. Critical factors influencing the polymerization rate, including pH 8.5-9, temperature 25-30°C, and DA concentration 0.1-2mg/mL, in addition to managing exposure to light. DA stock was made by dissolving 100 mg of DA in 1 mL of Milli-Q water. Subsequently, DA concentrations were diluted within the 0.25 to 2 mg/mL range in a solution in (0.1 M, pH 9± 0.3). The diluted solution was immediately prepared without exposure to light, just before injection into the microfluidic system. Various FRRs (1:1, 2:1, 3:1) were tested, along with TFR ranging from 10 to 20 mL/min. After microfluidic production, a filtration process was employed to remove ethanol and any unencapsulated DA, using TFF as described in the methods. The formulation was later kept at 25°C for 48 hours, and the resulting HLPs were stored at 2-8°C.

2.2.6. Drug Loading into HLPs

An initial PHT stock solution was prepared at 5 mg/mL in ethanol. This solution underwent dilution in PBS buffer (0.1 M with 1% Tween 20, pH 9 ± 0.3), yielding concentrations ranging from 0.1 to 0.8 mg/mL. Similarly, a stock solution of HA at 10 mg/mL in water was prepared and diluted in PBS buffer (0.1 M, pH 9 ± 0.3) to achieve concentrations from 0.1 to 0.8 mg/mL. Prior to injection into the microfluidic system, various concentrations of DA were promptly combined at different ratios, along with varied concentrations of either PHT or HA in fixed proportions with DA. Maintaining a pH of 9-8.5 (± 0.2), was crucial, and mixing occurred immediately before injection into the microfluidic system. In all formulations, a consistent lipid composition of DSPC, cholesterol, and DSPE-PEG -FA at a w/w ratio of 3:1:1 respectively (56:39:5 M ratio) was used. The HLPs were generated at a final concentration of 4 mg/mL after microfluidic, and all formulations underwent purification using TFF.

2.2.7. Physicochemical Characterization

2.2.7.1. Dynamic Light Scattering

The Zetasizer Ultra DLS was used to assess the particle size, PDI, and ZP of all nanoparticles (NPs). These analyses were conducted in triplicate at a temperature of 25 °C. To ensure accuracy, measurements were taken within the attenuation range of 6 to 9. Samples were suitably diluted at a 1:10 ratio using 0.1M of PBS buffer for size evaluations and Milli-Q water for ZP measurements. Each measurement set consisted of three independent replicates, and within each replicate, five measurements were performed. The average values were reported with their associated SDs.

2.2.7.2. UV-Vis Spectrophotometry

CloudSpec UV-Vis Spectrophotometer was used to characterize synthesized NPs across the wavelength range of 200 to 800 nm. Unlike conventional absorbance measurements, CloudSpec enabled the simultaneous measurement of extinction, absorption, and scattering, effectively eliminating turbidity interference. Additionally, the Multiskan SkyHigh Microplate Spectrophotometer from Fisher Scientific Limited was employed for UV-Vis absorbance measurements in microplates.

2.2.7.3. FT-IR Spectroscopy

To investigate the function groups within HLPs, Fourier transforms infrared (FT-IR) spectroscopy was applied. This analytical technique relies on the absorption of infrared radiation to explore the vibrational modes of molecules, by utilizing Shimadzu irSpirit FTIR spectrophotometers, recognized for their high sensitivity and resolution. The spectral range for the analysis spanned from 400 to 4000 cm^{-1}, covering the region where characteristic vibrational modes of diverse functional groups are typically observed. To ensure high-quality spectra, a resolution of 4 cm^{-1} was employed, capturing fine details in the absorption profile. Additionally, each sample underwent 64 scans, enhancing the signal-to-noise ratio and improving overall spectral quality.

2.2.7.4. Particle Tracking Analysis (PTA)

The size distribution of DiIC18-labeled HLPs nanoparticles suspended in 0.1 M PBS (pH 7.4 ± 0.3) was characterized using the NanoSight NS Pro system (Malvern Panalytical, Malvern, UK). The system was equipped with a 488 nm laser and a high sensitivity sCMOS camera to measure nanoparticle size distribution and estimated particle concentration. Samples were diluted to concentrations of 0.05–0.1 μg/mL and analyzed under constant flow at a rate of 1–1.5 μL/min using a syringe driver. Three video recordings were captured for each sample and averaged, with all analyses conducted at ambient temperature (~25 °C). Post-processing of the data was performed automatically using the NTA software (NS Xplorer), facilitating accurate analysis of particle trajectories.

2.2.8. Quantification of PHT and HA in HLPs

UV-spectroscopy was used to quantify PHT encapsulation in HLPs across varying concentrations. Standard solutions of PHT were prepared and analyzed at 218 nm. A standard curve was established, allowing for the quantification of PHT concentrations in the loaded HLPs. To measure the concentration of HA in HNPs, the carbazole assay was employed (Song, Im et al. 2009) Initially, HLPs-HA were prepared, along with a set of HA standards with known concentrations. Subsequently, the samples and standard concentrations were combined with 10% sulfuric acid in separate test tubes and subjected to hydrolysis at 100°C while stirring for 15 minutes. Upon complete hydrolysis, the samples and standards were allowed to cool to room temperature. Then each test tube received 100 μL of 1M sodium hydroxide per each mL of sample to neutralize the sulfuric

acid. Subsequently, the samples and standards were cooled to room temperature in the absence of light. Next, 100 µL of the samples or standard was added to the wells of the 96-well plate, Afterward, 10 µL of Carbazole solution (0.5 mg/mL carbazole stock) was added to the hydrolyzed mixtures. The samples were kept at a controlled temperature of 25°C for 20 minutes without exposure to light. Absorbance measurements were then recorded at a wavelength of 530 nm using the UV-Vis Spectrophotometer, and the absorbance values of the samples were compared to the curve generated from known HA standards concentrations.

2.2.9. Exploring Nanoparticle Stability Over 90 Days Storage

Liposomes and HLPs underwent a 3-month storage period at 4 ± 3 °C, and their stability was evaluated by monitoring essential physicochemical attributes, including average size, PDI, ZP, and size distribution, at different time intervals.

2.2.10. In Vitro biocompatibility evaluation of HLPs in dual cell lines: Viability assessment

This investigation involved a Cytotoxicity assessment of HLPs with FA viability assessments that were conducted using the Alamar Blue assay. HEK 293 and HeLa cell lines were systematically examined for the cellular Viability of loaded and empty HLPs, with and without FA conjugation. Cells were seeded at a density of 5,000 cells/well in the 96-well plates and cultured in DMEM with 10% FBS until reaching approximately 70-80% confluence. Following this, cells were exposed to different concentrations of HLPs (spanning from 1 to 400 µg/mL of the lipid weight) and incubated over 48 hours under controlled conditions at 37°C with 5% CO_2. After 48 hours of incubation, the media was gently removed and replaced by the addition of fresh cell culture media with 10% Alamar Blue reagent (v/v) and a subsequent 4-hour incubation at 37°C with 5% CO_2. Fluorescence measurements were acquired via GloMax® Microplate Readers – Promega at the wavelength (excitation: 520 nm, emission: 580-640 nm), cell viability was evaluated as a percentage relative to untreated control cells using a standard formula:

(1)

$$Cell\ viability\ (\%)\ =\ \frac{(FI(treated)-FI(blank))}{FI(control)-FI(blank)}*100\%$$

Where FI represents fluorescence intensity, and blank media only , and the control refers to the control without treatment.

The results are expressed as the mean value with its SD, derived from 10 replicates for each concentration across three independent batches.

2.2.11. In Vitro Release

The dialysis membranes were kept overnight in the dissolution medium to ensure thorough wetting prior to dialysis. For this study, Spectrum™ Labs 100 kD Biotech CE Dialysis Kits with a molecular weight cut-off (MWCO) of 100 kDa were employed to effectively retain the drug-loaded liposomes and HLPs while allowing smaller molecules to diffuse out. both forms made with the same lipid composition used in the liposomes with folic acid targeting. This protocol follows the method described by Saarinen-Savolainen et al (Saarinen-Savolainen, Järvinen et al. 1997) for evaluating drug release from liposomes under sink conditions. The following formulations were tested: liposomes loaded with HA, liposomes loaded with PHT, and HLPs containing a PDA polymer core with either HA or PHT in same encapsulation ratio. Two mL of each formulation in CD–Hepes (72 mM CD, 20 mM Hepes) were placed into each dialysis bag, which was then transferred into 45 mL of CD–Hepes solution at two different pH levels (pH 4 and pH 8). The solution inside the dialysis bag was stirred using a magnetic stirrer, while the external solution was agitated with an electric stirrer. As the experiment progressed, the volume of the sample in the dialysis bag changed due to the diffusion

of smaller molecules. Therefore, at each time point, the total volume in the dialysis bag was quantified, and the dilution factor was recalculated to ensure accurate data analysis. Samples of 200 µL were withdrawn at fixed time intervals from the external solution and replaced with equal volumes of fresh CD–Hepes solution to maintain a constant volume. The collected samples were analyzed to quantify the drugs at each time point, following the methods described in the analysis section for each loaded material.

2.2.12. Cellular uptake of HLPs

HLPs were systematically investigated for cellular uptake in HEK 293 and HeLa cell lines, encompassing loaded and empty HLPs with and without FA conjugation. The *in vitro* uptake process commenced with the seeding of cells following American Type Culture Collection (ATCC) guidelines, with a density of 10,000 cells per well in a 24-well plate. Cellular uptake was measured using 0.1% DiIC18 fluorescence dye encapsulated within the HLPs membranes. The cells were then incubated with 100 µg/mL HLPs- DiIC18 labelled of all forms in DMEM media treated with 10% FBS, And the control cell without treatment in the same condition and density, the FI of HLPs before incubation for the sample was quantified by GloMax® Microplate Readers – Promega at excitation wavelength of 520 nm and an emission wavelength of 580-640 nm, the cells were kept for incubation for 8 hours at 37°C with 5% carbon dioxide. Post-incubation, cell culture media were gently aspirated, and cells were washed five times with PBS (0.1M, pH 7.4 ± 0.3) to remove non-internalized HLPs. Subsequently, both treated and control cells were lysed with 1% Triton in PBS and kept at room temperature in darkness for 30 minutes. The FI after incubation of these cells is then quantified. The data is presented as the mean value with its SD, obtained from 10 replicates per each concentration.

(2)

$$Uptake\ \% \ = \ \frac{FI(HLPs\ after) - FI(control)}{FI(HLPs\ before) - FI(control)} * 100\%$$

Where FI denotes fluorescence intensity, and Control refers to untreated control cells.

2.2.13. Florescence imaging of fluorescent-labelled- HLPs

Fluorescent-labeled HLPs were subjected to fluorescence imaging to investigate the internalization of DiIC18-labeled HLPs in HEK 293 and HeLa cell lines. This analysis encompassed loaded and empty HLPs with and without FA conjugation. The experimental protocol involved seeding 10,000 cells in a glass-bottom confocal dish, permitting growth until reaching 70-80% confluency. Subsequently, the cell monolayer was incubated with HLPs labelled with DiIC18 (10 µg/mL) for 12 hours to prevent cell dislodgment after incubation, the cell culture media above the cells were gently aspirated, and the cells were washed several times using PBS (0.1M pH 7.4± 0.3) to remove non-internalized HLPs. Imaging was performed at 40 X magnification using the EVOS FL Colour Imaging System AMF 4300 microscope equipped with RFP 530 nm excitation and 593 nm emission filters, enabling the visualization of the difference from DiIC18-labeled HLPs internalization patterns within cells.

2.2.14. In Vitro Scratch Assay

The wound healing potential of HLPs with FA was assessed in HeLa cells through a scratch assay. Initially, HeLa cells were seeded in a 6-well plate and cultured in DMEM treated with 10% FBS until they reached 80-90% confluence (Walter, Wright et al. 2010). A 200L sterile pipette tip was used to create a controlled scratch into the cell monolayer.(Suarez-Arnedo, Figueroa et al. 2020). Subsequently, the cells were treated with

various samples, including the positive control (50 μM Quercetin) (Wang, Zhang et al. 2016), negative control (No treatment), 100 μg/mL HLPs, 100 μg/mL HLPs-PHT, and 100 μg/mL HLPs-HA. To optimize fluorescence imaging, all wells received 0.1% acridine orange. The treated cells were then incubated for 48 hours at 37°C with 5% carbon dioxide. Fluorescence microscopy was conducted for imaging using the Life Technologies EVOS FL Colour Imaging System AMF 4300 microscope equipped with GFP, 470 nm excitation, and 525 nm emission filters. The width of the scratch was quantified at different time intervals using Image J (NIH, Bethesda, MD). This facilitated the calculation of the percentage of wound closure, providing quantitative data on cell migration rate and wound healing percent over time (Suarez-Arnedo, Figueroa et al. 2020). The calculation formula employed in this study for assessing wound healing was expressed as

(3)

$$\%\, Wound\ healing\ =\ \frac{WSA(time\ 0) - WSA(time)}{WSA(time\ 0)} * 100\%$$

Where WSA represents the mean wound surface area; day 1 is the initial wound surface area, and the specific day refers to the wound surface area measured at a particular time (Deana, De Jesus et al. 2013).

2.2.15. Immunomodulation of Inflammatory Cytokines Using Enzyme-Linked Immunosorbent Assay

The immunomodulation of inflammatory cytokines was conducted through Adherence to the manufacturer's protocol was strictly maintained, An Enzyme-Linked Immunosorbent Assay (ELISA) (Chen, Chen et al. 2018) utilizing the BD Human IL-1β ELISA Set II (Cat. 557953) and Human TNF ELISA Set (Cat. 555212). HeLa cells were seeded in a 6-well plate and cultured in DMEM with 10% FBS until reaching 70-80% confluency (Walter, Wright et al. 2010). The cells were subjected to treatment with 5 ng/mL lipopolysaccharides (LPS) as a positive control (Minogue, Barrett et al. 2012), while negative control (No treatment), and the cells treated with empty HLPs, HLPs-PHT and HLPs-HA and incubated for 72 hours at 37°C with 5% CO_2, post-incubation, Supernatants from cell cultures were collected for the ELISA analysis.

2.2.15.1. Human TNF

In the ELISA procedure (Biosciences 2023), the monoclonal anti-human TNF-capture antibody was diluted in coating buffer (freshly prepared 0.1 M Na2CO at pH 9.5± 0.3). Subsequently, 100 μL of the diluted antibody was added to each ELISA plate well, followed by overnight incubation at 4°C. Washes with the wash Buffer (freshly prepared PBS solution with 0.05% Tween-20) were performed, and blocking ensued with the addition of 200 μL of Assay Diluent (freshly prepared PBS with 10% Fetal Bovine Serum (FBS) at pH 7.0). The PBS was precisely prepared with NaCl, Na2HPO4, KH2PO4, and KCL. Incubation for 1 hour at room temperature, followed by aspiration and three washes, was conducted. Subsequently, 100 μL of recombinant human TNF standard and samples were added to each well for a 2-hour incubation at room temperature. After aspiration and five washes with washing buffer, 100 μL of monoclonal biotinylated anti-human TNF detection antibody and streptavidin–horseradish peroxidase conjugate enzyme reagent (SAv-HRP) was added for 1-hour incubation at room temperature. The plate underwent five cycles of washing, and 100 μL per well of the Substrate Solution, including Tetramethylbenzidine (TMB) and Hydrogen Peroxide, was added, the plate was incubated in the dark for 30 minutes. Following this, Stop Solution (1 M H2SO4, 50 μL per well) was added, and absorbance was read at 450 nm with the UV-Vis Spectrophotometer within 30 minutes, with λ correction

at 570 nm. The data analysis involved constructing a calibration curve using absorbance values from standards. This curve served as a reference to calculating sample concentrations based on their respective absorbance data., determining cytokine concentrations.

2.2.15.2. Human IL-1β

The ELISA protocol for the BD OptEIA™ Human IL-1β ELISA Set II (Cat. 557953) (Biosciences 2023) closely parallels the TNF ELISA procedure and employs Coating Buffer, Assay Diluent, Wash Buffer, Substrate Solution, and Stop Solution. In this process, 100 µL of the Capture Antibody (Purified Anti-Human IL-1β), diluted in coating buffer, is added to each well of the ELISA plate, followed by an overnight incubation at 4°C. Subsequently, three washes with the washing buffer are performed. The plate is then blocked by the addition of 200 µL of Assay Diluent, with a 1-hour incubation at room temperature. After aspiration and three washes, 100 µL of Recombinant Human IL-1β Lyophilized Standards and samples are added to each well, and the plate is incubated at room temperature for 2 hours Following aspiration and five washes with washing buffer, 100 µL of Detection Antibody (Biotin Anti-Human IL-1β) is added for a 1-hour incubation at room temperature. After aspiration and five washes, 100 µL of SAv-HRP is added to each well, and the plate is incubated for 30 minutes. Following aspiration and seven cycles of washing the plate with 30-second soaks, 100 µL per well of the Substrate Solution (TMB) is added, and the plate is incubated in the dark for 30 minutes. The reaction is stopped with the addition of 50 µL of 1 M H2SO4 per well, and absorbance is read at 450 nm using the UV-Vis within 30 minutes, with λ correction at 570 nm. The data analysis utilized standards to create a calibration curve equation, allowing the calculation of sample concentrations from their absorbance values.

2.2.16. In Vivo wound healing study

The *in vivo* wound healing investigation was initiated with the isolation and acclimatization of 18 Sprague-Dawley female rats (200–300 g, aged 8-10 weeks) in a controlled environment for one week, maintaining standardized housing conditions. Subsequently, each rat underwent a surgical procedure, resulting in the creation of two 1.5 cm wounds on their upper neck. During the wounding procedure, mice were anaesthetized. To ensure objectivity and minimize bias, data analysis was conducted in a blind manner. Samples were coded, and the analyst remained unaware of the treatment groups until the data analysis was complete. For each sample, three rats were used. The control group was treated with 250 µL of PBS buffer 7.4± 0.3 daily for 14 days. The remaining rats were divided among various treatment groups. Each treatment group received a daily 250 µL application of a 2 mg/mL lipid concentration of both empty and loaded HLPs samples with FA for wound treatment. In the free drugs groups, the concentration calculated based on the concentration loaded FA-HLPs was applied via 250 µL for the diluted free drugs. This treatment regime continued for 14 days. A comprehensive daily data collection protocol was implemented, encompassing measurements of wound size, assessment of wound appearance, and general health observations. Throughout this process, strict adherence to ethical guidelines and approval from the relevant animal ethics committee were maintained. Continuous monitoring of the rats for signs of distress or discomfort ensured their welfare throughout the study. Post-wounding, daily topical application of HLPs was performed. Digital photographs of each wound were captured at designated time points for subsequent analysis. Daily data collection included wound size measurements, assessment of wound appearance, and general health observations. Wound area measurements were obtained through both ruler-based measurements and analysis using ImageJ software. Animal studies were conducted in strict accordance with the Guidance on the operation of the Animals (Scientific Procedures) Act 1986, the EU Directive 2010/63 for the protection of animals used for scientific purposes, and the NIH Guide for the Care and Use of Laboratory Animals. The protocols were approved by the ethical committee at Al-Zaytoonah

University (IRB number 01/05/2023-2024). The percentage of wound healing on a specific day was calculated based on the reduction of the wound surface area (WSA) using the formula:

(4)

$$\%\, Wound\ healing\ = \frac{WSA\ (day\ 1) - WSA\ (specific\ day)}{WSA(day\ 1)} * 100\%$$

Where WSA represents the mean wound surface area; Day 1 is the initial wound surface area, and the specific day refers to the wound surface area measured on that specific day.

2.2.17. Histological analysis

Skin tissue samples, preserved in 10% formalin, underwent histological preparation for analysis. The samples were sliced into 3-µm sections and subjected to hematoxylin and eosin (H&E) staining to visualize cellular structures. Subsequently, the stained sections were affixed onto glass slides for examination under a light microscope. To ensure impartial evaluation, a histopathologist, blinded to the experiment, assessed the stained sections using a Nikon ECLIPSE Ci light microscope (Tokyo, Japan). This method enabled the detailed examination of skin tissue morphology and any observable changes resulting from the 14-day nanoparticle treatment.

2.2.18. Data Collection and Statistical Analyses

The analysis comprehensively included parameters such as DLS repeated results, encapsulation efficiency, viability test dose-response, and the time-dependent progression of wound closure percentage among treated cells. Additionally, wound closure percentages were assessed at various post-surgery time points through repeated measurements. To ensure robustness, each experiment underwent three replications, with results presented as the means of the measurements ± SD and error bars indicating variability. Rigorous statistical analysis involved both one-way ANOVA and two-way ANOVA methods, followed by Tukey's multiple comparison test at a significance level of $p < 0.05$. In animal studies, the findings were specifically reported as the mean ± SD of three animals per sample, ensuring a comprehensive and precise presentation of the results.

3. Results and Discussion

3.1. Conjugation and characterization of FA for targeting

The conjugation process involved the reaction of the thiol group on DSPE-PEG-SH 2000 with the activated α-carboxyl group on the glutamic acid moiety of FA, facilitated by EDC/NHS (Sam, Touahir et al. 2010, Mani, Kim et al. 2018, Luo, Li et al. 2022), resulting in the formation of a thioester bond (DSPE-PEG-S-CO- FA) (Figure 1A). While conventional UV-spectroscopy typically shows minimal UV absorbance for DSPE-PEG-SH, the advanced optical design of CloudSpec UV-spectroscopy enabled simultaneous measurement of extinction and absorbance as a powerful tool for measuring turbid samples, with accurate absorption spectra and measures extinction, absorption, and scattering simultaneously. Post-synthesis and purification, UV-Vis

results displayed distinct peaks for DSPE-PEG-SH, FA, and the conjugation product. DSPE-PEG-SH exhibited a peak at 203 nm, while FA displayed peaks at 212 nm, 240 nm, 287 nm, and 365 nm (Baibarac, Smaranda et al. 2019, Li, Li et al. 2019). Post-conjugation, DSPE-PEG-FA exhibited peaks at 202, 211, 245, and 370 nm, confirming the successful synthesis and purification of the DSPE-PEG-FA conjugate (Figure 1B). This is consistent with previous research on absorption peaks for the DSPE-PEG-FA (Ghaznavi, Hosseini-Nami et al. 2018, Parvathaneni, Shukla et al. 2023). Complementing the UV-Vis spectroscopy findings, FTIR analysis in (Figure 1C) provided further confirmation of the successful conjugation of DSPE-PEG thiol with FA. The FTIR spectrum of the conjugated product exhibited two distinct peaks at 1683 cm^{-1} and 1735 cm^{-1}, unequivocally attributed to the formation of the thioester bond (O=C-S-R). These characteristic peaks signify the direct attachment of the FA moiety to the DSPE-PEG-SH by the thioester linkage. Additionally, the presence of a peak at 663 cm^{-1}, corresponding to the stretching vibration of the sulfur-carbon bond (C-S), further corroborates the successful conjugation process. Collectively, these FTIR data provide robust evidence for the formation of the desired DSPE-PEG-FA conjugate, further underscoring the reliability of the conjugation process. These findings align with those of Frigerio *et al*. (Frigerio, Bizzoni et al. 2019), emphasizing the robustness and reproducibility of DSPE-PEG-SH conjugation with FA observed in this investigation.

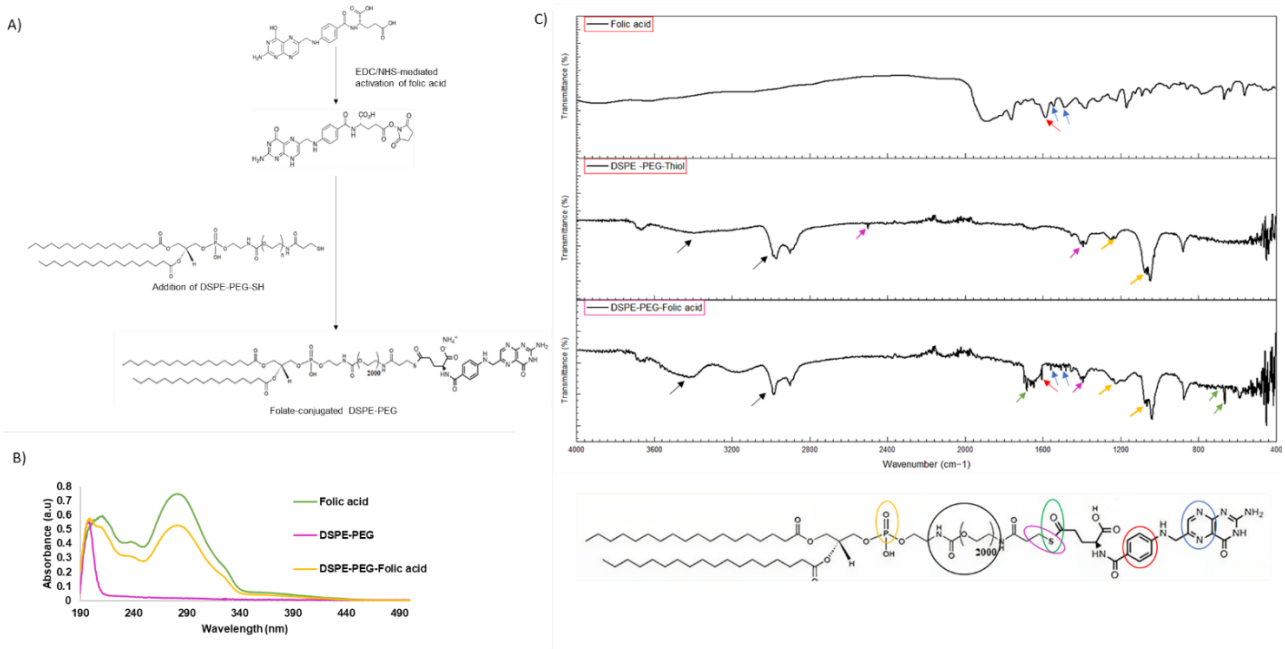

Figure 1. Multifaceted Analysis of FA Conjugation. A) Chemical reaction structure illustrating FA conjugation with DSPE-PEG-SH. B) UV-Vis absorbance profiles of DSPE-PEG-SH, FA, and DSPE-PEG -FA. C) FTIR spectra depicting FA, DSPE-PEG-SH, and Conjugated DSPE-PEG- FA.

3.2 Microfluidic Optimization of Liposome Formulation

Liposomes were synthesized using the NanoAssemblr® Benchtop system through microfluidic techniques, investigating various aqueous-to-lipid flow rate ratios (FRRs) of 2:1, 3:1, and 5:1, alongside total flow rates (TFRs) from 10 mL/min to 20 mL/min. At a constant TFR of 15 mL/min, increasing FRR significantly reduced average liposome size from 117.3 nm (± 3.56) to 72.64 nm (± 1.79) and PDI from 0.23 (± 0.015) to 0.14 (± 0.026) ($p < 0.05$), with ZP shifting from -9.65 mV (± 2.85) to -13.70 mV (± 1.74). Conversely, at a constant

FRR of 3:1, increasing TFR led to a decrease in average size from 82.59 nm (± 1.18) to 73.26 nm (± 1.15) ($p < 0.001$), with ZP shifting from -11.24 mV (± 2.14) to -14.24 mV (± 1.25). Additionally, for dopamine (DA)-loaded liposomes, increasing DA concentrations (0.5 mg/mL, 1 mg/mL, and 1.5 mg/mL) resulted in size increases from 85.67 nm (± 4.32) to 166.44 nm (± 5.21) and a decline in encapsulation efficiency (EE%) from 96.62% (± 2.78) at 0.5 mg/mL to lower values at higher concentrations. Optimal liposome characteristics, including maximum EE% of 94.65% (± 2.11), were achieved at a TFR of 20 mL/min. Supplementary Figure S1 and S2 provide detailed data supporting these findings, illustrating the influence of microfluidic parameters on liposome size, PDI, ZP, and encapsulation efficiency. These findings emphasize the critical role of microfluidic parameter optimization in tailoring liposome characteristics for specific applications.

3.3. Synthesis and Characterization of HLPs

The innovative approach to synthesizing PDA within liposomes leverages the unique adhesive and self-polymerization properties of DA, resulting in the formation of a PDA polymer inside the liposomal core. In a highly basic environment (pH 8-10), DA undergoes self-oxidation, generating PDA even under extremely low oxygen levels (Chen, Liu et al. 2017, Shalini Devi, Jacob et al. 2018), Notably, this distinct feature enables DA self-polymerization without relying on external catalysts, such as metal ions (Chen, Liu et al. 2017). While liposomes act as a partial barrier, they may not completely hinder the diffusion of small gases like oxygen (Wu, Bala et al. 2019). While liposomes act as a partial barrier, they may not completely hinder the diffusion of small gases like oxygen (Khan, Shanker et al. 2018).

In the liposome's alkaline core pH 9 (± 0.3), DA undergoes deprotonation and oxidation, leading to the formation of a reactive quinone intermediate. This intermediate then interacts with other DA molecules, initiating the formation of the PDA polymer. The self-polymerization process exhibits autocatalytic behavior, with the initial PDA serving as a catalyst for subsequent reactions (Chen, Liu et al. 2017, Khan, Shanker et al. 2018, Wu, Bala et al. 2019), where the PDA react with additional DA molecules, extending the PDA chain until complete polymerization. In this research the liposomal structure with a basic core establishes optimal conditions for DA self-polymerization, resulting in the spontaneous formation of a PDA polymer inside the core. Liposomes, especially those produced through microfluidic methods, provide a confined space that enhances EE% with controlled size and PDI. This synergistic process is both efficient and effective, leveraging DA reactivity and liposome protective characteristic s. A second advantage lies in PDA as pH-responsive behaviour, with stability in basic conditions and increased susceptibility to degradation in an acidic environment (Sun and Davis 2022). This property positions PDA as an excellent candidate for controlled drug delivery, allowing strategic triggering of drug release in an acidic condition. This has significant applications in drug delivery, such as the targeting release in acidic microenvironment in tumours (Cheng, Zhang et al. 2013, Sun and Davis 2022). Moreover, in topical applications, where the pH of healthy skin falls within the range of 5.5 to 7.4, and skin wounds exhibit increased acidity due to damaged blood vessels (Percival, McCarty et al. 2014), The PDA polymer, retaining the drug within liposomes, orchestrates a gradual and controlled release, with faster liberation in acidic environments and slower in basic conditions. This precisely regulated release mechanism presents substantial promise for enhancing drug delivery in wound healing contexts, providing customized release patterns attuned to the acidic microenvironment prevalent in skin wounds.

To prove the full polymerization after 24 hours, the FTIR analysis was employed again to scrutinize the polymer formation within liposomes at different stages: initially, before polymerization (time 0), and after 24 hours of DA self-polymerization. As illustrated in (Figure 2A) significant distinction was observed in the C-O stretching vibration band, transitioning from 1230-1240 cm^{-1} in liposomes with DA at time zero to 1270-1280 cm^{-1} in PDA after 24 hours of polymerization. This noteworthy shift corroborated the establishment of new C-O bonds during the polymerization of DA into PDA inside the liposome. Furthermore, an expanded peak in

the 2800-3400 cm^{-1} region for PDA, compared to liposomes with DA at time zero, was observed, indicating heightened concentrations of hydroxyl and amine groups in PDA. Additionally, distinctive peaks after 24 hours were identified for the C=O bond in the 1650 cm^{-1} region in PDA, and the N-C ring in the cyclic structure at 1273 cm^{-1}, and this confirms the polymerization of the all-free DA to form the HLPs, consistent with previous studies that have employed FTIR spectroscopy to characterize PDA and its derivatives (Yu, Chen et al. 2010, Chen, Liu et al. 2017), and these findings provided a comprehensive spectral profile of the evolving chemical bonds and functional groups during the polymerization process within the liposomal core

After identifying the optimal parameters for the microfluidic formation of FA -functionalized liposomes and determining the ideal concentration of DA with the highest EE%, these parameters were applied to produce HLPs. Maintaining a constant TFR of 20 mL/min and a FRR of 3:1 for the aqueous phase to lipid phase, 4 mg/mL of the lipid phase was combined with the aqueous phase containing 1 mg/mL of DA dissolved in PBS with a basic pH of 9 (± 0.3). The addition of DA in the microfluidic setup occurred immediately before the injection step into the system to ensure that DA would initiate the self-polymerization inside the liposome core after the formation of the liposome. Following microfluidic production, a filtration process was implemented to eliminate ethanol, which dissolved the lipid stock during the procedure, and any free DA outside the liposomes by tangential flow filtration system (TFF), as described in the methods section. (Figure 2B) shows the visible colour change after formulation after 24 hours, due to the oxidation of DA inside the liposome core.

The UV-Vis spectrum analysis revealed distinctive features providing insights into liposome composition. Empty liposomes (DSPC-Cholesterol-DSPE-PEG- FA) displayed absorption peaks at 200 nm and a small peak at 287 nm (Figure 2 C). In contrast, DA-loaded liposomes exhibited specific absorption peaks at 200 nm, 221 nm, and 284 nm, confirming the successful loading of DA after formulation and purification. After 24 hours, a new peak at 430-465 nm corresponding to the π-π^* transition within the aromatic ring, which is indicative of the formation of conjugated quinone and indoline structures during the self-polymerization process, served as a distinctive marker for PDA formation within the liposomes (Peterson, Le-Masurier et al. 2014). Additionally, the loading efficiency after formulation was calculated by establishing a calibration curve using standard concentrations of free DA and free PDA.

The Dynamic Light Scattering (DLS) results (Figure 2D, E, and F) unequivocally demonstrate a notable increase in liposome size upon loading with DA, shifting from 72.36 nm (± 2.6) to 93.66 nm (± 1.25). Remarkably, the ZP remains consistent with no significant change after loading, indicating that DA is encapsulated within the liposomes, and the loading process does not alter the surface properties. The size distribution intensity, as shown in Figure 2 D, exhibits no significant shift after loading (time zero), and post-polymerization at 24 and 48 hours, indicating stability in size after polymerization within the liposomes over time. The same holds for the ZP, showing no significant shift in surface charge after full polymerization at 24 and 48 hours the size and PDI after formulation and 48 hours have no significant changes. This compelling finding strongly supports the occurrence of the self-polymerization process within the liposomes, emphasizing that this process maintains the liposomes' structural integrity without altering their surface properties. The visible transition from the initial colourless or pale-yellow state to a dark brown or black hue is a reliable indicator, aligning seamlessly with the UV-Vis and FTIR findings. These comprehensive results collectively affirm and validate the successful DA polymerization, providing a robust foundation for further understanding and applications in drug delivery systems. Our study brings forth a novel perspective by centering on the self-polymerization of DA within the liposomal matrix. This inventive strategy holds promise for achieving a more stable and controlled release form of nanoparticles, representing a significant advancement in HLPs drug delivery systems not previously reported in existing literature. Unlike previous research, which primarily

delved into the polymerization of PDA or its coating application (Deng, Shang et al. 2018, Ryu, Messersmith et al. 2018, Palladino, Bettazzi et al. 2019), our work distinguishes itself by developing the HLPs as a biocompatible polymer with pH sensitivity for drug release within the liposome.

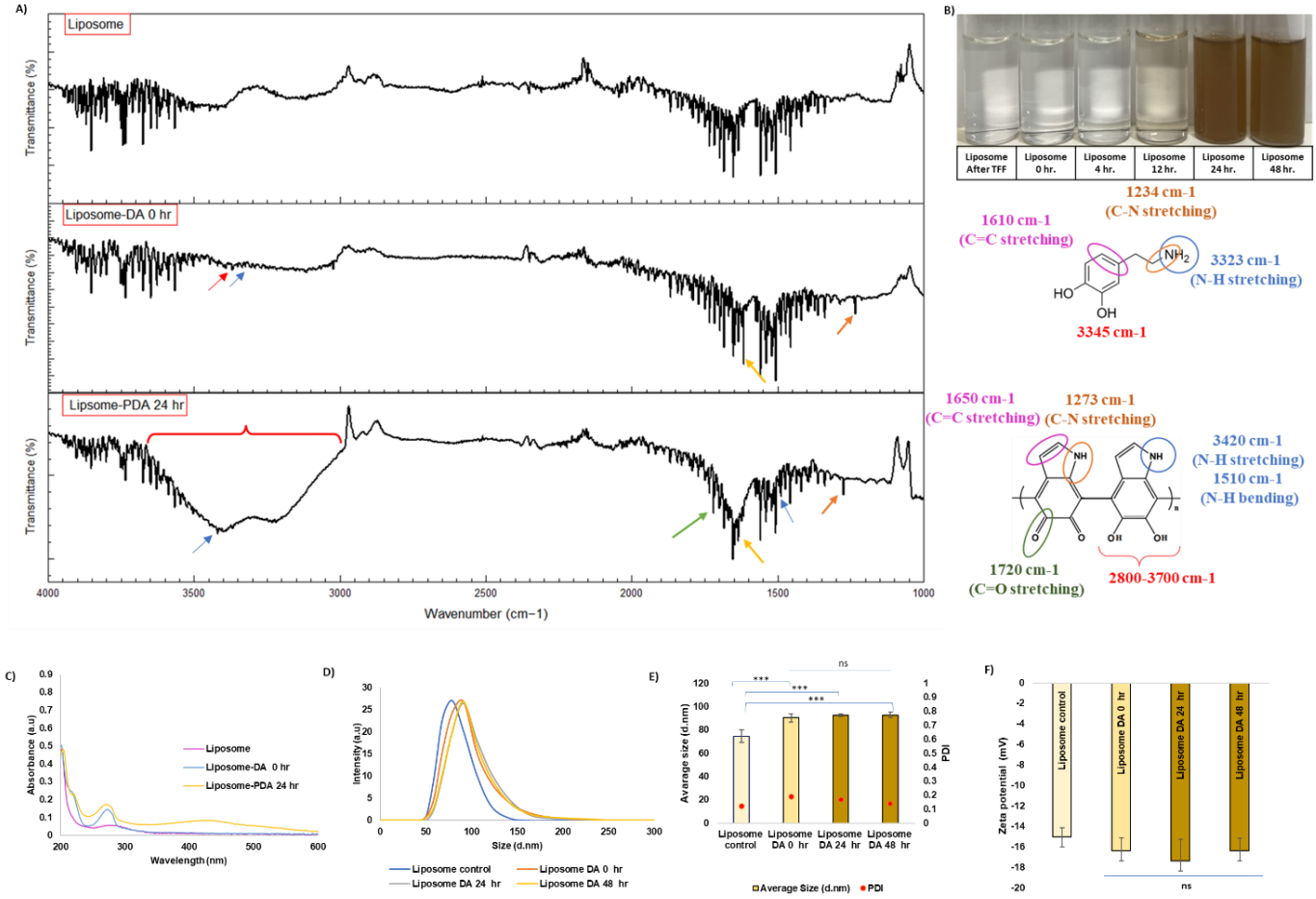

Figure 2. Evaluation of liposome characteristics before and after dopamine loading and PDA polymerization. A) FTIR spectra for empty liposome, liposome loaded with dopamine at time 0, and after 24 hours of Polymerization. B) Images represent liposomes at time 0, 4 hours, 12 hours, 24 hours, and 48 hours C) UV-VIS Results. D) Size distribution intensity before loading, after loading at time 0, and After PDA Polymerization at 24 hours and 48 hours E) Size and PDI. F) Zeta Potential. The outcomes are derived from the average values obtained from at least three independent batches, with error bars representing the SD. Non-significant differences are denoted as ns (Not Significant, $p > 0.05$). Significant differences are indicated as follows: *$p < 0.05$, **$p < 0.01$, and ***$p < 0.001$.

3.4. Drug Loading into HLPs

The microfluidic manufacturing system exhibits high efficiency in producing loaded drugs (Roces, Lou et al. 2020). Leveraging the process of DA polymerization and its strong adhesion properties, the resulting polymer stabilizes materials and drugs within (Kim, Gim et al. 2014, Lynge, Schattling et al. 2015), rendering the HLPs system an excellent drug delivery platform with remarkable drug stability. The minimal loss or release of drugs outside the target site makes it particularly promising for loading various pharmaceutical forms with poor

pharmacokinetic properties or even biological materials, serving as a targeted stabilization and release system (Sunoqrot, Bae et al. 2011).

Taking advantage of this synergistic effect, DA and drugs were co-loaded prior to encapsulation within targeted liposomes with FA, and their performance was monitored post-transformation into HLPs. Both drugs and loaded DA were dissolved in a basic medium, aligning with the manufacturing parameters established in previous sections. The system's ability to carry drugs at high concentrations without compromising their properties was investigated. To determine the optimal concentration for encapsulation efficacy, various drug to lipid ratios were tested under fixed conditions (TFR of 20 mL/min and FRR of 3:1 for the aqueous phase to the lipid phase) as the best parameter for this formulation. The lipid phase (4 mg/mL) was combined with the aqueous phase, containing concentrations of DA (0.5 or 1 mg/mL), and (0.1-0.8mg/mL) of either PHT or HA.

The results depicted in Figure S3 highlight a noticeable correlation between the physicochemical properties and HLPs loading ratios, the HLPs loaded with varying ratios of DA-PHT displayed a discernible size augmentation (Figure S3A), ranging from 89.11 nm (± 3.22) to 312.86 nm (± 17.26), indicative of a size-dependent response to DA-PHT loading ratios. Correspondingly, the ZP of HLPs-PHT formulations exhibited fluctuations (Figure S3B), reflecting alterations in surface charge with different DA-PHT ratios, ranging from -9.36 mV (± 1.36) to -19.47 mV (± 3.37).

Similarly, HLPs loaded with diverse DA-HA ratios showcased a size increment relative to the control (Figure S3C), elucidating the impact of DA-HA loading on liposomal size 71.79 nm (± 3.65) to 259.81 nm (± 12.36). The ZP of HLPs-HA formulations displayed variations (Figure S3D), underscoring changes in surface charge with varying DA-HA ratios, ranging from -16.36 mV (± 2.39) to -29.36 mV (± 3.97). EE% for PHT and DA demonstrated variability with loading ratios (Figure S3E), pinpointing optimal conditions for encapsulation. Notably, higher DA-PHT ratios correlated with reduced EE%, suggesting a potential saturation effect. Like PHT, the EE% for HA and DA exhibited a dependence on loading ratios (Figure S3F). The post-filtration drug recovery outcomes underscore robust retention capabilities for both PHT and HA (Figure S3G), with negligible losses during the filtration process. Particle recovery after syringe filtration shows the efficacy of the purification process (Figure S3H), revealing high recovery percentages for both HLPs-PHT and HLPs-HA.

Emphasizing the focus on identifying optimal ratios that do not alter the physicochemical properties of the HLPs, the DLS results for HLPs loaded with either PHT or HA exhibit relatively similar behavior. The findings reveal that the ratio preserving HLPs size and charge is observed at a ratio of 0.5:0.2 DA-drug. Results for HLPs-PHT include a size of 100.115 nm (±5.32), PDI of 0.13 (±0.02), ZP of -15.15 (±1.42), EE% PHT at 91.26 (±2.5), and EE% DA at 89.99 (±1.7). Similarly, HLPs-HA displays comparable values: 103.51 nm (±4.21) in size, PDI of 0.11 ±0.03, ZP of -16.36 (±2.85), EE% HA at 94.48 (±4.5), and EE% DA at 85.57 (±3.2). This loading percentage, of both DA and the drug, is approximately 17% w/w of the lipid, representing a remarkably high proportion. Our conclusion emphasizes the capability of microfluidics to achieve efficient and high drug-loading percentages. Importantly, the results confirm that loading did not adversely affect particle parameters or properties, maintaining an average size within the 100nm range with a PDI below 0.2, without altering the surface charge.

3.5. Stability Assessment of Liposomes and HLPs during Prolonged Storage

The comprehensive stability assessment of liposomes and HLPs yielded promising results, demonstrating their suitability for long-term storage and use. The standardized production process through a microfluidic system contributed to consistent NPs characteristics.

Throughout the entire 90-day study period illustrated in Figure 3, both liposomes and HLPs displayed remarkable stability. Liposomes maintained an average particle size range of 80–120 nm (Figure 3A), with a PDI consistently below 0.29 (± 0.05) (Figure 3B) with an acceptable range of ZP (-16 to -10 Mv) (Figure 3C). Similarly, HLPs maintained an average particle size of 95–105 nm (Figure 3D), with a low PDI below 0.22 (± 0.06) (Figure 3E). The ZP remained within acceptable ranges for HLPs, ranging from -14 to -12 mV (Figure 3F). Remarkably, HLPs exhibited a narrower range of ZP values and average sizes compared to liposomes, suggesting higher stability. This observation is in line with previous studies demonstrating the superior ability of PDA to enhance stability and reduce susceptibility to aggregation (Yang, Liu et al. 2018). Overall, the conducted stability study reaffirms the preservation of physicochemical attributes, including particle size and distribution, in liposomes, particularly those incorporating the polymer, even during prolonged storage and exposure to conditions mimicking the physiological environment.

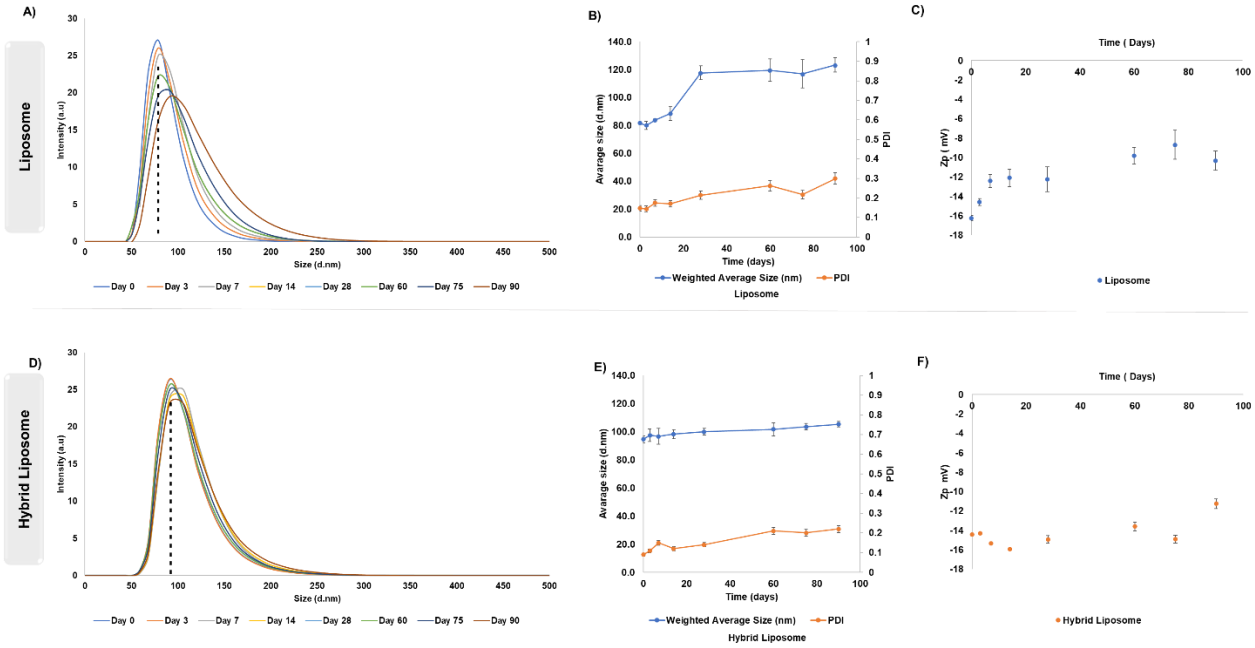

Figure 3. Stability test of liposomes and HLPs at 4 °C over 3 months. A) Liposome size distribution intensity plots. B) Liposome particle size and polydispersity. C) Liposomes ZP. D) HLPs size distribution intensity plots., E) HLPs particle size and polydispersity. F) HLPs ZP. Results represent the mean of at least 3 independent batches, and the SD is plotted as error bars**.**

3.6. Particle Tracking Analysis (PTA):

The NanoSight Pro (NS Pro), equipped with a 488 nm laser and a high-sensitivity sCMOS camera, was employed for Nanoparticle Tracking Analysis (NTA) to characterize the size distribution of DiIC18-labeled liposomes and DiIC18-labeled HLPs (Figure 4). This system effectively measured particle diameters across a wide range, including the mean particle size as well as the D10, D50, and D90 distributions, while showing minimal batch-to-batch variation. Although NTA is semi-quantitative due to the requirement for frequent

dilutions, it proved to be highly reliable for characterizing particle sizes in this study. In Figure 4, we present NTA concentration vs. DLS intensity plots for DiIC18-labeled nanoparticles. Panels (A) DiIC18-Empty Liposome, (B) DiIC18-HLPs, (C) DiIC18-HLPs-HA, and (D) DiIC18-HLPs-PHT illustrate the size distributions measured using both NTA-Fluorescence and NTA-Scatter modes, with D10, D50, and D90 values displayed alongside DLS measurement results. The analysis in both light scattering and fluorescence modes revealed consistent size distributions, confirming that the Fluorescence Labelling Efficiency - Concentration [%] was derived from liposome-sized particles. The formula used for span, Span = (D90 - D10) / D50, demonstrated a low span value, indicating a monodisperse population and confirming the uniformity of both liposomes and HLPs. No additional peaks suggestive of micelle formation or aggregation were observed, supporting the efficient encapsulation of DiIC18 dye within the liposome membranes. Representative images captured by the NanoSight Pro sCMOS camera are shown in Figure S4, which provides NanoSight Pro camera images displaying the DiIC18-labeled particle distributions for (a) DiIC18-Empty Liposome, (b) DiIC18-HLPs, (c) DiIC18-HLPs-HA, and (d) DiIC18-HLPs-PHT, as visualized during NTA analysis.

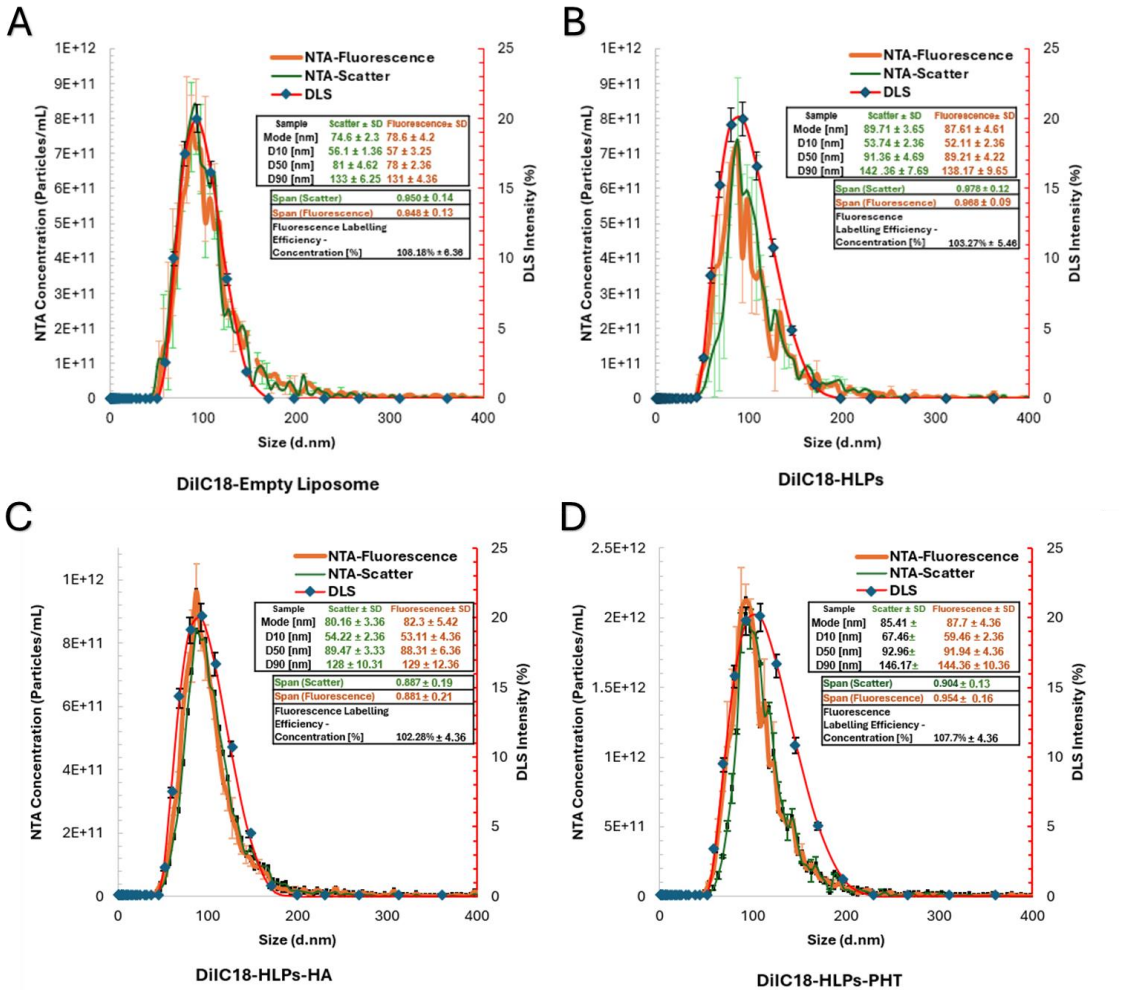

Figure 4. Particle Tracking Analysis concentration vs. Dynamic Light Scattering (DLS) intensity plots of DiIC18-labeled nanoparticles, with detailed size distributions including D10, D50, and D90 values. (A) DiIC18-Empty Liposome, (B) DiIC18-HLPs, (C) DiIC18-HLPs-HA, and (D) DiIC18-HLPs-PHT. Each panel presents size distributions measured by both NTA-Fluorescence and NTA-Scatter modes. The data includes Scatter ± SD and Fluorescence ± SD for Mode, D10, D50, and D90 values for each sample. Additionally, Span

values for Scatter and Fluorescence are provided, along with the Fluorescence Labelling Efficiency - Concentration [%] for each sample, offering a comprehensive characterization of particle uniformity and labeling efficiency.

3.7 Release Profiles of Conventional and Hybrid Liposomes at pH 4 and pH 8

In this study, we evaluated the release profiles of two formulations: conventional liposomes and HLPs loaded with hyaluronic acid (HA) or phenytoin in same ratio. The release at both pH 4 and pH 8 are illustrated in Figures 5A and B, respectively.

At pH 4, conventional liposomes exhibited rapid drug release, with approximately 76.87% of phenytoin released within 12 hours and 83.50% released by 24 hours. Specifically, the release at 6 hours was 71.53% for liposomes containing phenytoin and 71.39% for those containing HA. The data, averaged from three replicates, showed minimal variation, with standard deviations indicating consistent replicability. This rapid release can be attributed to effective diffusion facilitated by the stirring conditions during the dialysis process.

In contrast, the HLPs, which incorporate a polydopamine polymer core, demonstrated a slower and more sustained release profile. At 12 hours, only 42.53% of phenytoin was released from the HLPs at pH 4, while the release increased to 49.39% by 24 hours. The presence of the polydopamine polymer likely contributes to the moderation of drug diffusion, enhancing formulation stability and prolonging the release profile compared to conventional liposomes.

The comparative analysis of both pH levels highlights the influence of the surrounding environment on drug release dynamics. The significance of prolonged drug release is particularly relevant in the context of wound healing. Sustained release formulations can maintain therapeutic concentrations of drugs at the site of injury, which is crucial for effective treatment and healing. Studies have shown that sustained release of therapeutic agents, such as growth factors and anti-inflammatory drugs, can enhance wound healing by promoting tissue regeneration and reducing inflammation (Ashraf, Lee et al. 2009, Rohner, Nguyen et al. 2020). At pH 8, conventional liposomes exhibited a similar rapid release pattern, with 67.65% of phenytoin released after 12 hours and 77.05% after 24 hours. The release percentages were lower than those observed at pH 4, which may be due to increased pH affecting liposomal structure and drug solubility. Notably, the hybrid liposomes at pH 8 also demonstrated gradual release, with approximately 20.63% of phenytoin released by 24 hours, indicating a robust mechanism that slows down drug release compared to conventional formulations.

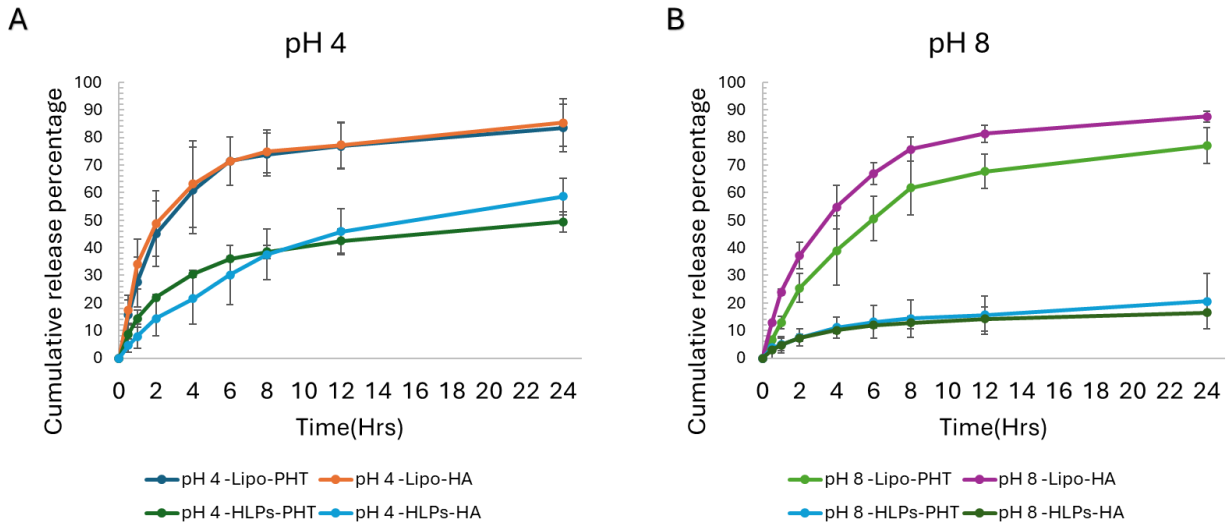

Figure 5. Release Profiles of Conventional Liposomes and HLPs Loaded with Phenytoin and Hyaluronic Acid at (A) pH 4 and (B) pH 8.

3.8. Cellular Uptake and Cytocompatibility of FA-Conjugated HLPs

The outcomes of this study showcase a comprehensive analysis of DiIC18-labeled loaded and empty HLPs, exploring both viability and cellular uptake.

The investigation includes a comparison of both targeted (FA-conjugated) and untargeted formulations in HEK 293 and HeLa cell lines, as shown in Figure 6. Figures 6A and B, show fluorescence microscopy RFP images visually depict the uptake of labelled- HLPs in HEK 293 and HeLa Cells, respectively, offering a tangible insight into the cellular behaviour of HLPs. In Figure 6C, the result of DiIC18-labeled HLPs delves into a comparison between FA-conjugated (HLPs-FA) and unconjugated formulations in both HeLa and HEK 293 cells after an 8- hour incubation. The FI data were collected and analyzed using the GloMax® Microplate Reader- Promega, yielding average uptake percentages with corresponding SDs and p-values for each formulation.

In HeLa cells, the uptake percentages for unconjugated formulations were as follows: Empty HLPs 64.36% (± 6.64), HLPs-HA 65.62% (± 4.52), and HLPs-PHT 64.26% (± 3.46). Similarly, in HEK 293 cells, the uptake percentages for unconjugated formulations were as follows: Empty HLPs 61.36% (± 5.63), HLPs-HA 59.90% (± 5.99), and HLPs-PHT 56.35% (± 4.74). indicating an absence of significant differences in cellular uptake between HeLa and HEK 293 cells within the unconjugated formulations with FA.

On the other hand, comparing HLPs-FA and unconjugated formulations in HeLa cells, the uptake percentages were as follows: Empty HLPs 64.36% (± 3.64), Empty HLPs -FA 89.36% (± 13.23), HLPs-HA 65.62% (± 6.52), HLPs-FA-HA 87.52% (± 7.72), HLPs-PHT 64.26% (± 4.46), and HLPs-FA-PHT 86.24% (± 6.28). Statistical analysis indicated significant differences between Empty HLPs and Empty HLPs-FA ($p < 0.001$), HLPs-FA-HA and HLPs-HA ($p < 0.001$), and HLPs-FA-PHT and HLPs-PHT ($p < 0.01$).

Meanwhile, in HEK 293 cells, the uptake percentages were as follows: Empty HLPs 61.36% (± 2.63), Empty HLPs -FA 61.74% (± 4.50), HLPs-HA 59.90% (± 2.99), HLPs-FA-HA 58.10% (± 7.82), HLPs-PHT 56.35%

(± 3.74), and HLPs-FA-PHT 61.54% (± 5.87). No significant differences were observed in uptake between any of the HLPs formulations in HEK 293 cells.

The cellular uptake study revealed that FA-conjugation significantly enhanced the cellular uptake of DiIC18-labeled HLPs in HeLa cells but not in HEK 293 cells. In HeLa cells, FA-conjugation resulted in an increased uptake of Empty HLPs, HLPs-PHT, and HLPs-HA, with percentage enhancements of approximately 25%, 22%, and 33%, respectively. The one-way ANOVA analysis revealed a highly significant difference in cellular uptake among the treatment groups ($p < 0.0001$). The F value was 16.07, with 11 and 24 degrees of freedom for treatment and residual, respectively. The R-squared value of 0.8805 indicates that 88.05% of the variance in cellular uptake can be explained by the model.

This enhanced uptake can be attributed to the overabundance of FRs on HeLa cells, which readily bind to FA, facilitating the internalization of FA-conjugated HLPs (Holm, Hansen et al. 2000, Soleymani, Azizi et al. 2021). HeLa cells are known to express high levels of FRs, which are essential for their rapid proliferation and nutrient uptake (Soleymani, Azizi et al. 2021). FA serves as a ligand for these receptors, and its conjugation onto HLPs effectively exploits this receptor-mediated endocytosis mechanism to enhance cellular uptake. Conversely, in HEK 293 cells, no substantial difference in uptake was observed between FA -conjugated and unconjugated HLPs. This suggests that FA conjugation may not be an effective strategy for enhancing cellular uptake in this cell line. HEK 293 cells express lower levels of FRs compared to HeLa cells, resulting in a reduced ability to internalize FA -conjugated HLPs (Hansen, Greibe et al. 2015, Yoshitomi, Nakayama et al. 2020, Soleymani, Azizi et al. 2021).

The viability of both loaded and empty HLPs targeted with FA was evaluated through the Alamar Blue assay. Figures 6D and E illustrate the dose-response viability tests in HeLa and HEK 293 cells. In HEK 293 cells, Empty HLPs, HLPs-HA, and HLPs-PHT exhibited diverse percentages relative to the control, demonstrating minimal cytotoxic effects, particularly noticeable at high concentrations. Similarly, in HeLa cells, both loaded and empty formulations, whether HLPs-HA or HLPs-PHT, displayed negligible cytotoxicity, with adverse effects observed only at elevated concentrations. The results highlight the promising potential of FA-conjugated HLPs for safe and precise drug delivery. The results reveal a substantial enhancement in cellular uptake facilitated by FA conjugation in HeLa cells, aligning with the study's primary objective of augmenting the targeted effectiveness of these nanoparticles towards FRs. This improved uptake mechanism relies on FR-mediated internalization, offering a promising pathway for significantly enhancing drug delivery, particularly targeting the skin. Notably, the observed heightened cellular uptake is accompanied by minimal cytotoxicity exhibited by both loaded and empty FA-conjugated HLPs, further confirming their overall safety and potential for diverse biomedical applications, this observation is in line with a previous studies that reported a significant increase in the uptake of FA-conjugated nanoparticles in HeLa cells compared to non-targeted nanoparticles indicating the specificity of the targeting approach (Mansoori, Brandenburg et al. 2010).

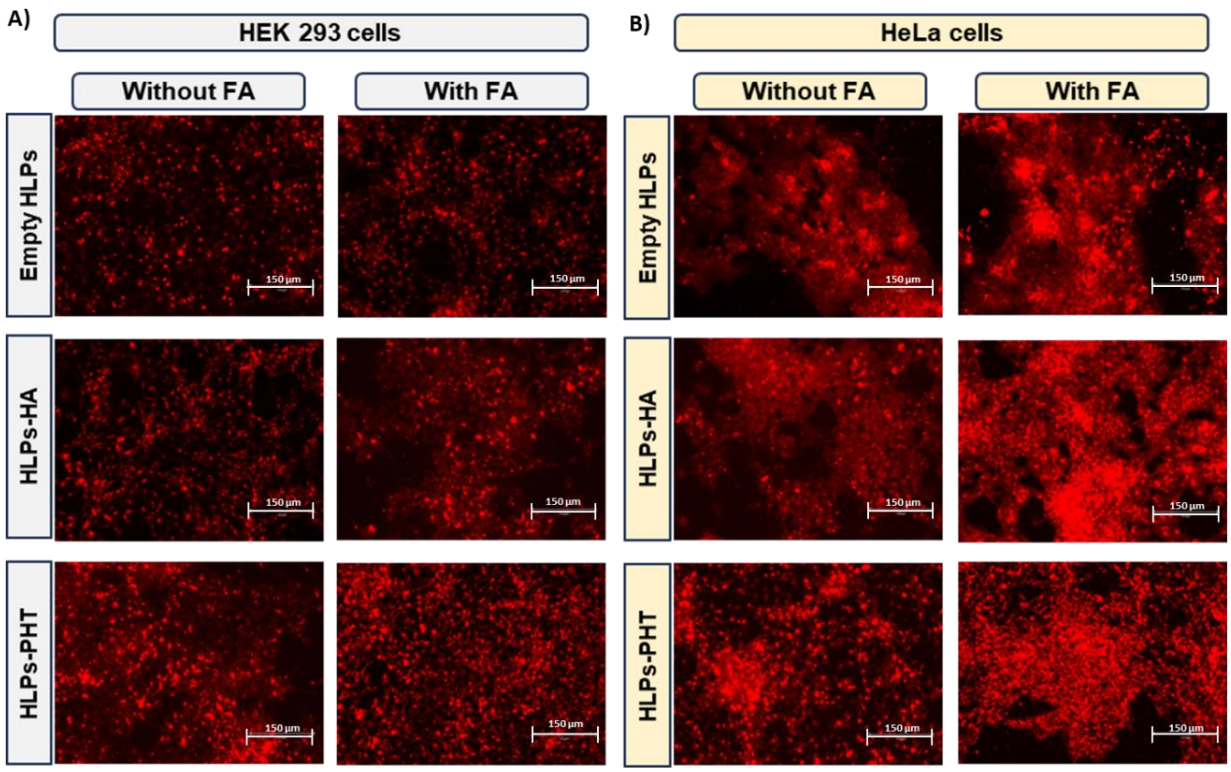
A)
HEK 293 cells
Without FA
With FA
Empty HLPs
HLPs-HA
HLPs-PHT
B)
HeLa cells
Without FA
With FA
Empty HLPs
HLPs-HA
HLPs-PHT
150 µm

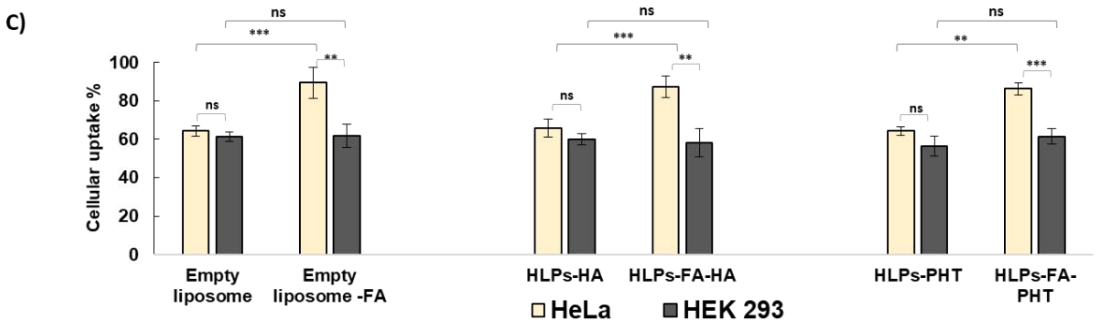
C)
Cellular uptake %
100
80
60
40
20
0
ns
***
**
Empty liposome
Empty liposome -FA
HLPs-HA
HLPs-FA-HA
HLPs-PHT
HLPs-FA-PHT
HeLa
HEK 293

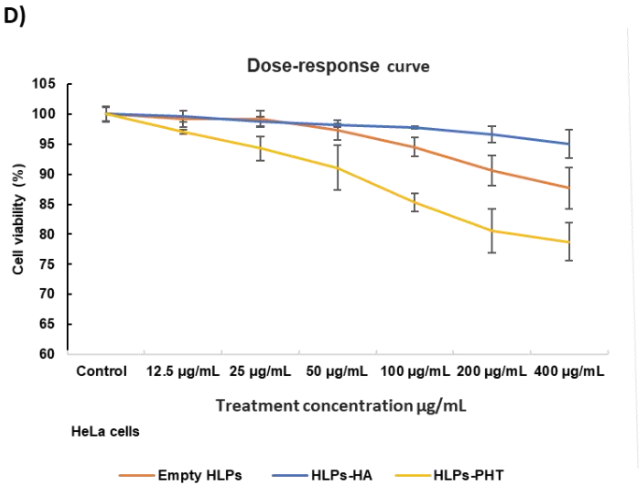
D)
Dose-response curve
Cell viability (%)
105
100
95
90
85
80
75
70
65
60
Control
12.5 µg/mL
25 µg/mL
50 µg/mL
100 µg/mL
200 µg/mL
400 µg/mL
Treatment concentration µg/mL
HeLa cells
Empty HLPs
HLPs-HA
HLPs-PHT

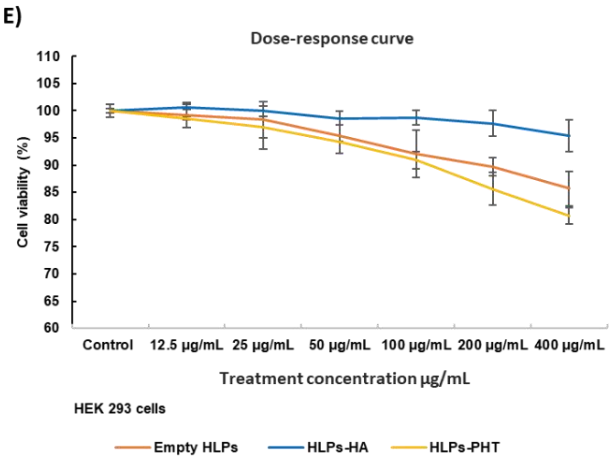
E)
Dose-response curve
Cell viability (%)
110
105
100
95
90
85
80
75
70
65
60
Control
12.5 µg/mL
25 µg/mL
50 µg/mL
100 µg/mL
200 µg/mL
400 µg/mL
Treatment concentration µg/mL
HEK 293 cells
Empty HLPs
HLPs-HA
HLPs-PHT

Figure 6. Comparative *in vitro* analysis of DiIC18-labeled loaded and empty HLPs viability and cellular uptake, with and without FA conjugation in HEK 293 and HeLa cell lines. (A) EVOS fluorescence microscopy RFP image of labeled-HLPs uptake in HEK 293 cells. (B) EVOS fluorescence microscopy RFP image of labeled-HLPs uptake in HeLa cells. (C) Uptake percentages in both cell lines. (D) Viability test dose-response in HeLa cells for FA- HLPs (E) Viability test dose-response in HEK 293 cells for FA- HLPs. Results are based on the mean values from a minimum of 3 independent batches, and error bars indicate SD. Non-significant differences are denoted as ns (Not Significant, $p > 0.05$). Significant differences are indicated as follows: *$p < 0.05$, **$p < 0.01$, and ***$p < 0.001$.

3.9. *In Vitro Scratch Assay and Inflammatory Cytokines*

This assay serves as an initial indication of the potential of these formulations in promoting wound healing, underscoring its significance in the early stages of dermatological drug development. In evaluating the wound healing potential of HA and PHT-loaded HLPs, a scratch assay was conducted on HeLa cells. The assessment involved comparing wound healing dynamics to both negative controls (No treatment) and quercetin treated as positive control. Figure 7A shows the fluorescence microscopy images taken at various time points (0, 12, 24, and 48 hours) following HLPs treatment for cells labeled with acridine orange. The Life Technologies EVOS FL Colour Imaging System was employed for image capture, and measurements were carried out using ImageJ tools, as detailed in the method section. Quantification of wound closure percentages at various time intervals, as depicted in Figure 7B, facilitated the evaluation of wound healing progress which plays an important role in evaluating the *in vitro* wound healing ability of HLPs-PHT and HLPs-HA.

Scrutinizing various formulations over 48 hours revealed distinctive trends, with the negative control consistently achieving 100% closure, affirming experimental reliability. The Empty HLPs exhibited a wound closure profile like the negative control, suggesting no discernible contribution to the wound healing effect. The HLPs-HA formulation exhibited enhanced closure compared to the empty HLPs, aligning with the known regenerative roles of HA(D'Agostino, Maritato et al. 2019). The exceptional efficacy of the HLPs-PHT formulation was evident, achieving an impressive 95.19% closure within 24 hours and complete healing within just 48 hours. This rapid closure suggests that the formulation could harness the inherent wound-healing properties of PHT, potentially enhancing its therapeutic effectiveness *in vitro*. These findings are consistent with previous studies (Sayar, Gergerlioglu et al. 2014, Liu, Li et al. 2016) which have highlighted PHT's ability to accelerate wound closure by stimulating fibroblast proliferation and collagen synthesis. Such recognition emphasizes the potential integration of PHT into HLPs to facilitate improved wound recovery.

To unravel the intricate mechanisms governing skin wound healing, ELISA antibody tests were employed for precise quantification of inflammatory cytokines(Biosciences 2023). Utilizing HeLa cells facilitated a thorough analysis of cell-specific responses to these cytokines, providing insights into their crucial influence on fundamental cellular behaviors essential for wound healing(Lin, Calvano et al. 2000). Tumor necrosis factor (TNF), a pro-inflammatory cytokine, plays a vital role in the process. Optimal TNF levels are beneficial, fostering inflammation, promoting growth factor production, and enhancing cell migration, proliferation, and survival. However, prolonged exposure to elevated TNF levels can be detrimental, diminishing extracellular matrix production and encouraging metalloproteinase synthesis. This dual role highlights the concentration-dependent impact of TNF on wound healing, emphasizing the need for a delicate balance to ensure effective tissue restitution and regeneration (Barrientos, Stojadinovic et al. 2008, Ritsu, Kawakami et al. 2017). On the

other hand, interleukin-1beta (IL-1β) is implicated in wound healing, sustaining a continuous proinflammatory wound macrophage phenotype, and hindering the process.

Mirza *et al*. [61] reveals the increased IL-1β expression and secretion observed in wounds from both diabetic individuals and mice, contributing to inflammation and impairing tissue repair. In diabetic mice wounds, inhibiting the IL-1β pathway promotes a transition from a pro-inflammatory to a healing-associated macrophage phenotype, leading to enhanced expression of wound growth factors and expedited healing (Mirza, Fang et al. 2013, Sidaway 2015, Wang, Zhang et al. 2020). Understanding the delicate balance between IL-1β and other cytokines is crucial for understanding the complexities of the wound healing process (Mirza, Fang et al. 2013, Nosenko, Ambaryan et al. 2019).

Figure 7 C, D illustrates variations in IL-1β and TNF levels among treatments with the HLPs, and LPS as positive control. Specifically, TNF levels show a significant increase in the PHT-loaded HLPs compared to the negative control, while IL-1β levels display a notable decrease, approaching values similar to the negative control, this unique pattern implies a specific impact of PHT on immune signaling pathways, potentially influencing components of the wound healing process. The observed elevation in TNF levels is consistent with TNF's recognized pro-inflammatory effects, which, in turn, promote an efficient wound healing process by facilitating tissue repair and remodeling, modulating macrophage polarization, and enhancing angiogenesis (Brockmann, Giannou et al. 2017). However, the reduction in IL-1β levels prompts further exploration, considering the known role of IL-1β in wound healing. Mirza *et al*.(Mirza, Fang et al. 2013) demonstrated that high IL-1β can sustain a proinflammatory wound macrophage phenotype, potentially hindering wound healing. Therefore, the observed decrease in IL-1β levels in PHT-treated cells may indicate a specific influence of PHT on this pathway, potentially promoting aspects of the wound healing process.

On the other hand, TNF levels in HA-treated cells are notably lower than those treated with PHT, indicating a distinct immunomodulatory profile. The slightly elevated IL-1β levels in HA-treated cells suggest a potential involvement in the initial inflammatory phase crucial for initiating tissue repair (Shini, Shini et al. 2020). The balance of pro-inflammatory and regenerative effects illustrates the multifaceted role of HA in the wound healing process, with supported evidence highlighting its potential as a therapeutic agent for effective tissue repair and regeneration (Kaul, Short et al. 2021). Distinctive immunomodulatory effects of PHT and HA-loaded HLPs on TNF and IL-1β levels were revealed. An increase of TNF in PHT and decreased IL-1β suggests possible benefits for wound healing. Previous studies by Putra *et al*. indicated that TNF stimulation enhances wound healing (Putra, Ibrahim et al. 2022), while research by Dai *et al*. demonstrated that a high level of IL-1β can impede the healing process (Dai, Shen et al. 2021). However, it is worth mentioning that HA presents a distinct signature, which has reduced TNF as well as a slight increase in IL-1β, indicating a different mechanism. Through these insights, it is possible to appreciate how PHT and HA loadings differ and interact with an immune response to influence wound healing and tissue regeneration.

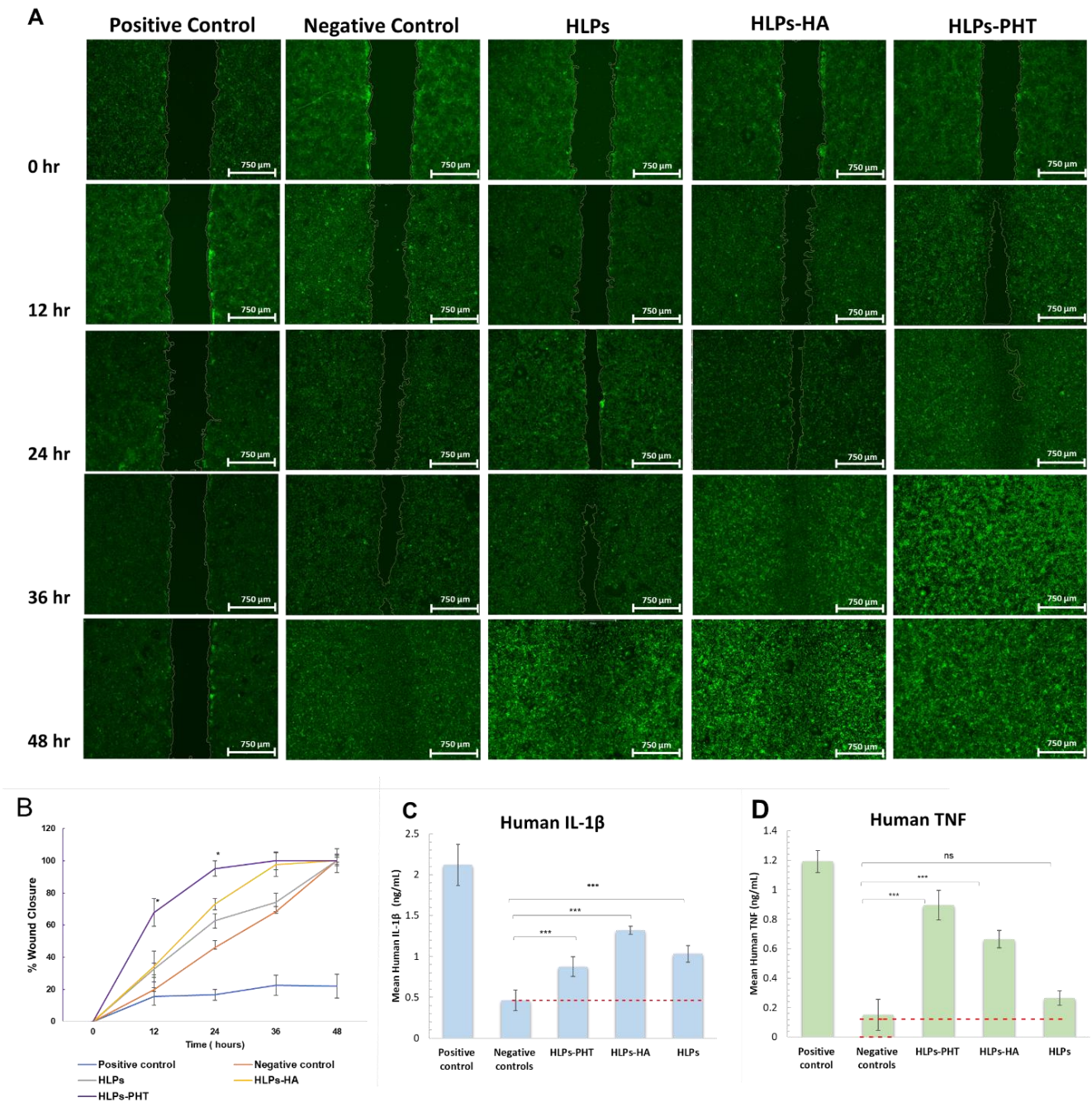

Figure 7 (A) Fluorescence microscopy GFP Imaging of HeLa cells labelled with acridine orange fluorescence dye, depicting wound closure over time in positive and negative controls, and HLPs empty and loaded at different time points. (B) Statistical values of wound closure percentage over time in treated cells. (C) IL-1β secretion levels in HeLa cells treated with HLPs; (D) TNF secretion levels in HeLa cells treated with HLPs. Results represent the mean values from 4 independent batches, and error bars indicate SD. Non-significant differences are denoted as ns (Not Significant, $p > 0.05$). Significant differences are indicated as follows: *$p < 0.05$, **$p < 0.01$, and ***$p < 0.001$.

3.10. In vivo Wound Healing Study

Full-thickness wounds were carefully induced on the backs of 28 female rats, subsequently categorized into control and treatment groups. The treatment groups underwent daily treatments for 14 days. Rigorous data collection, following strict ethical guidelines, encompassed wound size measurements, appearance assessments, and general health observations. For enhanced precision and result confirmation, wound areas were meticulously calculated using ImageJ software from digitally captured photographs at specific time points. Quantitative data, substantiated by visual observations, affirmed a notable reduction in wound inflammation, oedema, and granulation tissue formation within the treated groups.

Only the FA conjugated form was used, and the presented findings delineate the wound closure progression percentages over 14 days for various treatments, providing valuable insights into their effectiveness. In the control group, a gradual closure is observed, reaching 96.52% by day 14, emblematic of natural healing. The findings in Figure 8A indicate that both PHT-loaded and HA-loaded HLPs significantly accelerated wound healing compared to the control groups. The panel displays representative images of skin wounds treated with PBS 0.1M pH 7.4 ± 0.3 (control), free PHT, free HA, empty HLPs, HLPs-HA, and HLPs-PHT over the treatment period.

In Figure 8B, quantitative analysis displays wound closure percentages at different post-surgery time points for free forms, empty HLPs, and HLPs loaded with HA and PHT, the analysis at specific time points unveils the accelerated closure achieved by HLPs-PHT, surpassing other treatments on day 3 with 65.12% (± 6.21) and maintaining its lead on day 4 with 70.19% (± 3.84). This trend persists on day 5 with 86.22% (± 5.12) and day 7 with 94.61% (± 2.57), consistently outperforming other groups. Notably, on day 10, HLPs-HA and HLPs-PHT demonstrated impressive closure percentages of 96.13% (± 2.09) and 100%, respectively, highlighting the robust wound-healing potential of the HLPs system, especially when loaded with PHT. These results highlight the promising therapeutic applications of HLPs-PHT for efficient wound healing, showcasing its superior performance compared to other treatments. On the other hand, HLPs-HA exhibits competitive wound closure rates at 69.24% (± 4.47), 85.75% (± 2.73), and 87.23% (± 4.55) on days 5, 7, and 8, respectively. While not matching the exceptional performance of HLPs-PHT, it consistently outperforms Free HA, Free PHT, and Empty-HLPs groups. Figure 8C highlights a comparison between the free drug forms and the HLP-loaded forms of PHT and HA, revealing significant differences with p-values < 0.05 when examining HLPs-HA against the free form of the drug on day 7. Similarly, Figure 8D contrasts HLPs-PHT with the free form of PHT on days 3, 4, and 5, indicating significant differences with p-values < 0.05. Figure 8E unveils notable differences in wound closure between HLPs-PHT treatment and the untreated control group on days 3 and 4, with p-values < 0.05 and < 0.01 for day 5. The significantly higher closure rates in HLPs-PHT emphasize its effectiveness in accelerating wound healing. These results demonstrate the significance of HLPs in tissue repair, positioning them as a promising therapeutic avenue. Impressive *in vitro* wound healing, reduced cytokine expression, and remarkable *in vivo* efficacy establish HLPs-PHT as a leading candidate for wound healing.

Novel microfluidic development of pH-responsive hybrid liposomes

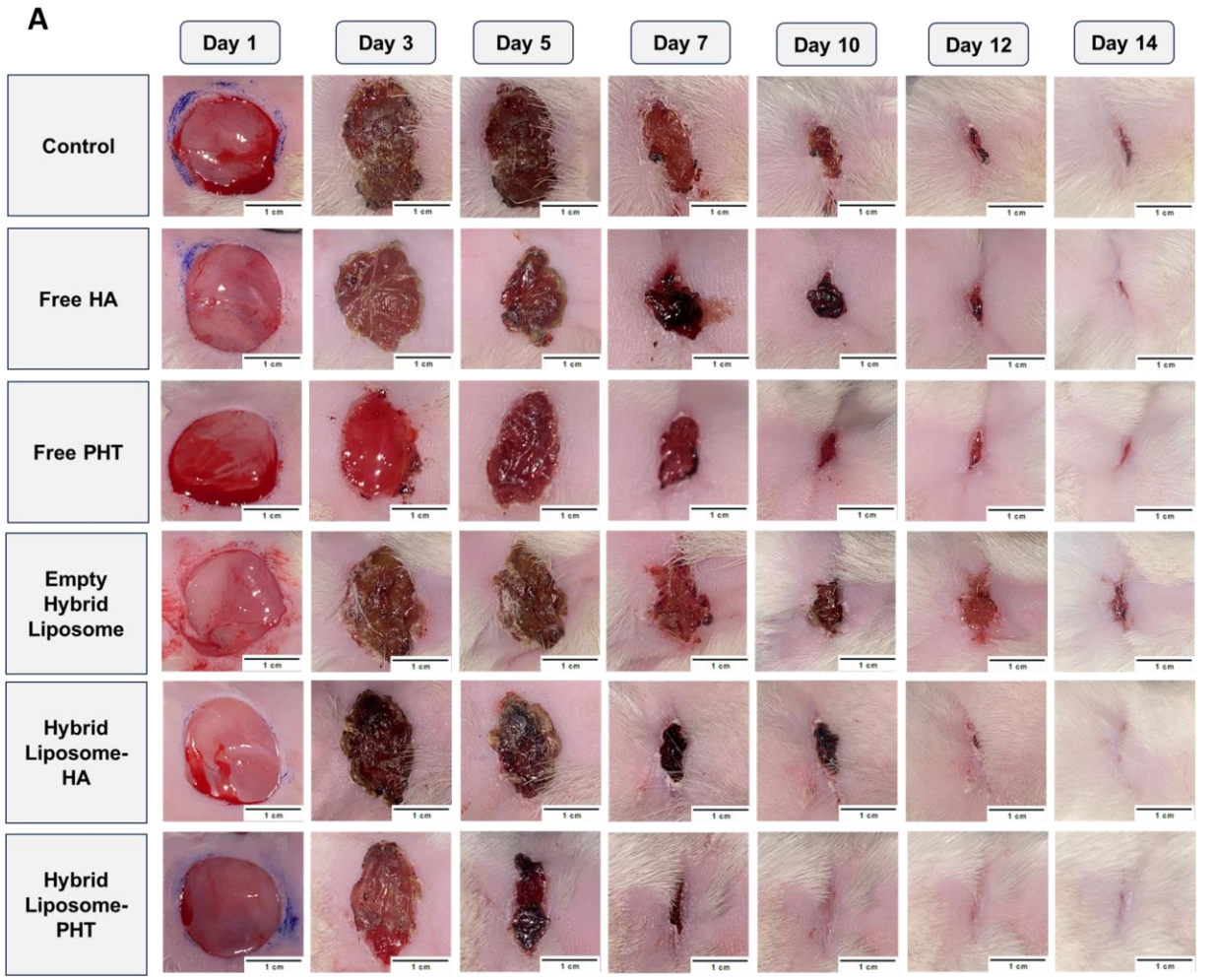

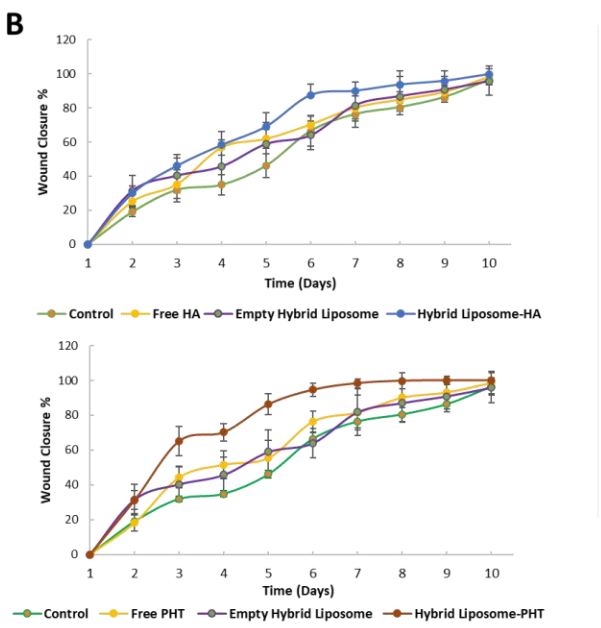

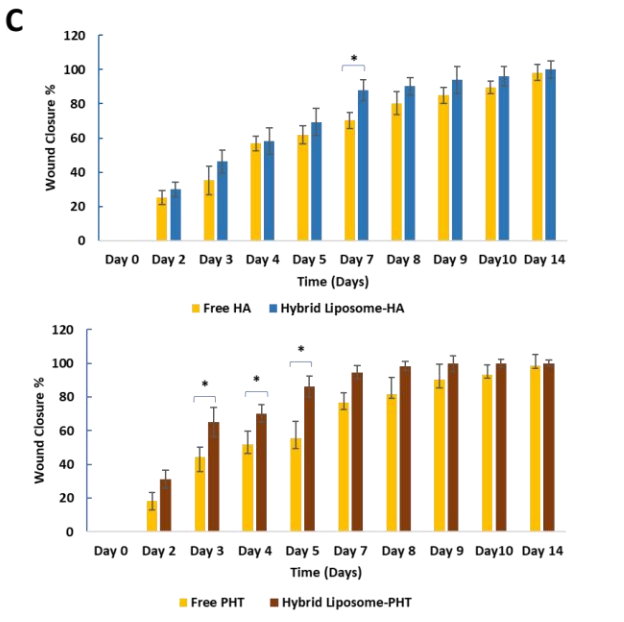

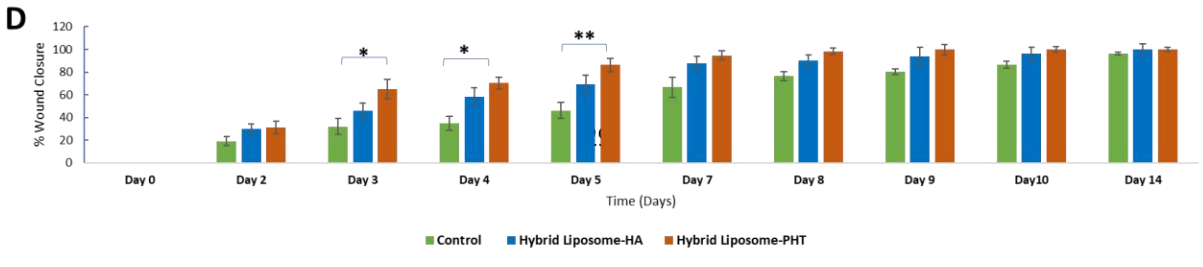

Figure 8. (A) Representative images showing skin wounds treated with PBS 0.1M pH 7.4 ± 0.3 as a control, free PHT, free HA, empty HLPs, HLPs-HA, and HLPs-PHT over the course of the treatment days. (B) Quantitative analysis displaying wound closure percentages at different post-surgery time points for free forms, empty HLPs, and HLPs loaded with HA and PHT. (C) A comparison between the free drug forms and the HLP-loaded forms of PHT and HA. (D) Differences in wound closure between HLPs-PHT and HLPs-HA compared to the control group. Results are based on the mean values from a minimum of four independent batches, with error bars representing SD. Non-significant differences are marked as ns (Not Significant, $p > 0.05$), while significant differences are indicated as follows: *$p < 0.05$, **$p < 0.01$, and ***$p < 0.001$.

3.11. Histological Responses to Wound Treatments

Histological analysis unveiled diverse responses to various treatments. The control group (PBS) exhibited minimal healing progress, showing focal ulceration and edema (Figure 9A). In contrast, free HA showcased encouraging signs of wound repair, characterized by hyperkeratosis, diverse polymorphs, and lymphocyte presence (Figure 9B). Similarly, free PHT treatment demonstrated features indicative of tissue repair, including a thinner epidermis and minimal vascular fibrous tissue (Figure 9C). However, empty HLPs resulted in a slower healing process, marked by cellular damage (hydropic degeneration) and a weak inflammatory response (minimal inflammatory cell infiltration) (Figure 9D). Interestingly, treatment with HLPs-HA revealed ongoing healing with underlying vascular connective tissue, suggesting a potentially distinct mechanism of action compared to free HA alone (Figure 9E). HLPs-PH elicited the most complex response, with both inflammation and tissue alterations observed alongside the presence of fibrous tissue, potentially indicating complete healing in some areas (Figure 9F). Overall, both free HA and PHT demonstrated promising results, suggesting their potential as therapeutic agents for wound repair. While HLPs-HA exhibited similar healing effects to free HA, some histological differences suggest potential modifications in the delivery system are warranted. Additionally, the complex response observed with HLPs-PH emphasizes the need for further investigation into its mechanism of action and potential synergistic effects.

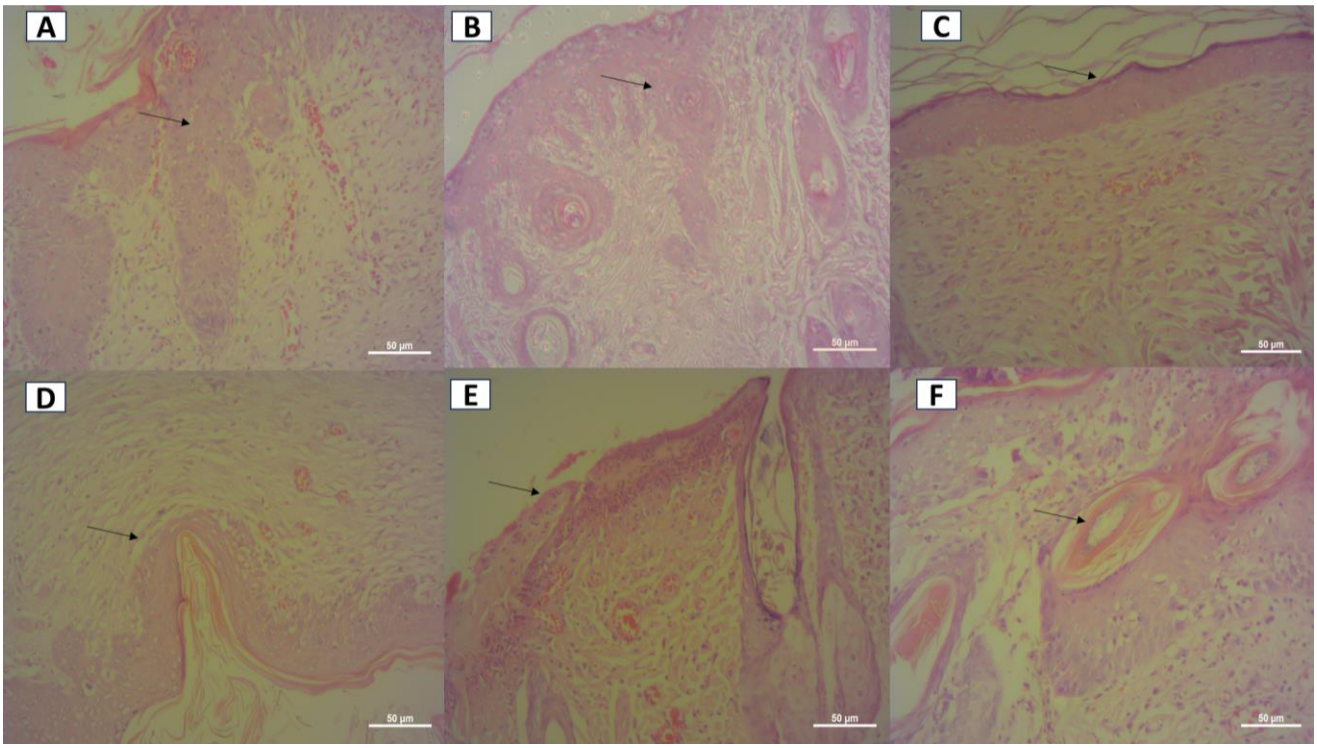

Figure 9. Representative images illustrating the histological examination of skin wounds after a 14-day treatment duration. The treatments comprise (A) PBS 0.1M pH 7.4 ± 0.3 as a control, (B) free HA, (C) free PHT, (D) empty HLPs, (E) HLPs-HA, and (F) HLPs-PHT.

4. Conclusions

In summary, this research thoroughly investigated the versatile potential of FA targeting, and the successful optimization of conjugated FA liposome formulation through microfluidic techniques using the NanoAssemblr® Benchtop system was accomplished in a distinct phase of the study. The investigation focused on the effects of different FRR and TFR on liposome characteristics, revealing a significant impact on size, PDI, and ZP. The precise control and optimization of microfluidic parameters demonstrated their crucial role in tailoring liposome properties for specific applications. The investigation primarily focused on assessing the contributions of HLPs to wound healing and antibody activation, holding potential implications for chronic wounds. Meticulous conjugation and characterization of FA with DSPE-PEG-SH confirmed through UV-Vis and FTIR analyses, affirmed successful synthesis and reproducibility through microfluidic fixed parameters. Also, an innovative approach to DA polymerization within the liposomal structure, forming PDA, was developed, exhibiting advantages such as efficient encapsulation and pH-responsive behavior, particularly beneficial in acidic wound environments. The stability study over 90 days reinforced the resilience of liposomes and HLPs, emphasizing their suitability for long-term storage and use. A comprehensive assessment of *in vitro* compatibility and cellular uptake of FA-conjugated HLPs, in both empty and loaded forms, supports the therapeutic potential of the approach. Notably, *in vivo* wound healing studies in a rat model conclusively demonstrate the superior efficacy of HLPs -PHT, highlighting the robust effects of the HLPs system for drug delivery, whether incorporating PHT or HA. The exceptional wound closure efficacy of HLPs, as evidenced in rat studies, emphasizes their potential as a potent, antibiotic-free drug delivery system for wound healing. These results collectively propel our comprehension of microfluidic optimization for HLPs formulations,

opening avenues for cutting-edge drug delivery systems applicable in controlled release and targeted therapies. This study marks a significant breakthrough in wound healing treatments by introducing a versatile drug delivery platform that overcomes the limitations of traditional liposomal drug delivery systems. The research illustrates the transformative potential of targeted HLPs through microfluidic technology in revolutionizing wound healing, instilling fresh optimism for effective treatment.

Author contributions: CRediT

The authors contributed to this study as follows: Conceptualization was jointly led by Yvonne Perrie and Hakam Alaqabani. Hakam Alaqabani was responsible for the formulation development of the nanoparticles, the chemical modification of the lipid, and the execution of *in vitro* experiments, as well as data curation and formal analysis. Funding acquisition and investigative efforts were conducted by Alaa Hammad. The project administration and resource management were overseen by both Yvonne Perrie and Alaa Hammad. Animal work was carried out by Yara Abosnwber. The original draft of the manuscript was prepared by Hakam Alaqabani, with all authors contributing to the writing, review, and editing. All authors have reviewed and approved the final version of the manuscript.

Declaration of Competing Interest

The authors declare that they have no competing financial interests or personal relationships that could have influenced the work reported in this paper. Specifically, none of the authors have any employment, consultancies, stock ownership, honoraria, paid expert testimony, patent applications, registrations, grants, or other funding that could be perceived as potential conflicts of interest.

Funding

This work was supported by the University of Strathclyde, Glasgow, UK, and the Al-Zaytoonah University of Jordan, Amman, Jordan [Grant No. 26/12/2019-2020].

Acknowledgments

Special thanks are extended to Professor Suhair Sunoqrot for her support, as well as to Panida Punnabhum, Muattaz Hussain, Ankita Borah, and the Yvonne Perrie lab group for their invaluable support.

Declaration of generative AI and AI-assisted technologies in the writing process

During the preparation of this work, the author(s) used Grammarly to improve grammar and spelling. After using this tool, the author(s) reviewed and edited the content as needed and take(s) full responsibility for the content of the published article.

References

Al-Jamal, W. T. and K. Kostarelos (2011). "Liposomes: from a clinically established drug delivery system to a nanoparticle platform for theranostic nanomedicine." Accounts of chemical research **44**(10): 1094-1104.

Ashraf, A., P. H. Lee, K. Kim, V. Zaporojan, L. Bonassar, R. Valentini, A. Spangenberger, J. J. P. Weinzweig and r. surgery (2009). "Effect of sustained-release PDGF and TGF-β on cyclophosphamide-induced impaired wound healing." **124**(4): 1118-1124.

Avishai, E., K. Yeghiazaryan and O. Golubnitschaja (2017). "Impaired wound healing: facts and hypotheses for multi-professional considerations in predictive, preventive and personalised medicine." EPMA Journal **8**: 23-33.

Bai, Q., K. Han, K. Dong, C. Zheng, Y. Zhang, Q. Long and T. Lu (2020). "Potential applications of nanomaterials and technology for diabetic wound healing." International journal of nanomedicine: 9717-9743.

Baibarac, M., I. Smaranda, A. Nila and C. Serbschi (2019). "Optical properties of folic acid in phosphate buffer solutions: the influence of pH and UV irradiation on the UV-VIS absorption spectra and photoluminescence." Scientific Reports **9**(1): 14278.

Barrientos, S., O. Stojadinovic, M. S. Golinko, H. Brem and M. Tomic-Canic (2008). "Growth factors and cytokines in wound healing." Wound repair and regeneration **16**(5): 585-601.

Biosciences, B. (2023). "BD OptEIA™ Human IL-1β ELISA Set II protocol." BD Biosciences.

Biosciences, B. (2023). "BD OptEIA™ Human TNF ELISA Set protocol." BD Biosciences.

Brockmann, L., A. D. Giannou, N. Gagliani and S. Huber (2017). "Regulation of TH17 cells and associated cytokines in wound healing, tissue regeneration, and carcinogenesis." International journal of molecular sciences **18**(5): 1033.

Chen, T.-P., T. Liu, T.-L. Su and J. Liang (2017). "Self-polymerization of dopamine in acidic environments without oxygen." Langmuir **33**(23): 5863-5871.

Chen, Y.-J., M. Chen, Y.-C. Hsieh, Y.-C. Su, C.-H. Wang, C.-M. Cheng, A.-P. Kao, K.-H. Wang, J.-J. Cheng and K.-H. Chuang (2018). "Development of a highly sensitive enzyme-linked immunosorbent assay (ELISA) through use of poly-protein G-expressing cell-based microplates." Scientific reports **8**(1): 17868.

Cheng, F.-F., J.-J. Zhang, F. Xu, L.-H. Hu, E. Abdel-Halim and J.-J. Zhu (2013). "pH-sensitive polydopamine nanocapsules for cell imaging and drug delivery based on folate receptor targeting." Journal of biomedical nanotechnology **9**(7): 1155-1163.

Colombo, C., M. Li, S. Watanabe, P. Messa, A. Edefonti, G. Montini, D. Moscatelli, M. P. Rastaldi and F. Cellesi (2017). "Polymer nanoparticle engineering for podocyte repair: from in vitro models to new nanotherapeutics in kidney diseases." ACS omega **2**(2): 599-610.

D'Agostino, A., R. Maritato, A. La Gatta, A. Fusco, S. Reale, A. Stellavato, A. V. A. Pirozzi, M. De Rosa, G. Donnarumma and C. Schiraldi (2019). "In vitro evaluation of novel hybrid cooperative complexes in a wound healing model: a step toward improved bioreparation." International Journal of Molecular Sciences **20**(19): 4727.

Dai, J., J. Shen, Y. Chai and H. Chen (2021). "IL-1β impaired diabetic wound healing by regulating MMP-2 and MMP-9 through the p38 pathway." Mediators of Inflammation **2021**: 1-10.

Deana, A. M., S. H. C. De Jesus, B. P. A. Sampaio, M. T. Oliveira, D. F. T. Silva and C. M. França (2013). "Fully automated algorithm for wound surface area assessment." Wound Repair and Regeneration **21**(5): 755-761.

Deng, Z., B. Shang and B. Peng (2018). "Polydopamine based colloidal materials: synthesis and applications." The Chemical Record **18**(4): 410-432.

Ejeta, F. (2021). "Recent advances of microfluidic platforms for controlled drug delivery in nanomedicine." Drug Design, Development and Therapy: 3881-3891.

Farook, F. F., M. N. M Nizam and A. Alshammari (2019). "An update on the mechanisms of phenytoin induced gingival overgrowth." The Open Dentistry Journal **13**(1).

Fischer, M. J. (2010). "Amine coupling through EDC/NHS: a practical approach." Surface plasmon resonance: methods and protocols: 55-73.
Frigerio, B., C. Bizzoni, G. Jansen, C. P. Leamon, G. J. Peters, P. S. Low, L. H. Matherly and M. Figini (2019). Folate receptors and transporters: biological role and diagnostic/therapeutic targets in cancer and other diseases, Springer.
Ghaznavi, H., S. Hosseini-Nami, S. K. Kamrava, R. Irajirad, S. Maleki, A. Shakeri-Zadeh and A. Montazerabadi (2018). "Folic acid conjugated PEG coated gold–iron oxide core–shell nanocomplex as a potential agent for targeted photothermal therapy of cancer." Artificial cells, nanomedicine, and biotechnology **46**(8): 1594-1604.
Hansen, M. F., E. Greibe, S. Skovbjerg, S. Rohde, A. C. Kristensen, T. R. Jensen, C. Stentoft, K. H. Kjær, C. S. Kronborg and P. M. Martensen (2015). "Folic acid mediates activation of the pro-oncogene STAT3 via the Folate Receptor alpha." Cellular signalling **27**(7): 1356-1368.
Holm, J., S. I. Hansen, M. Høier-Madsen, L. Korsbaek, H. Beckmann and K. Josefsen (2000). "Ligand binding characteristics of a glycosylphosphatidyl inositol membrane-anchored HeLa cell folate receptor epitope-related to human milk folate binding protein." Bioscience Reports **20**(2): 109-118.
Kaul, A., W. D. Short, S. G. Keswani and X. Wang (2021). "Immunologic roles of hyaluronan in dermal wound healing." Biomolecules **11**(8): 1234.
Khan, Z., R. Shanker, D. Um, A. Jaiswal and H. Ko (2018). "Bioinspired polydopamine and composites for biomedical applications." Electrically Conductive Polymer and Polymer Composites: From Synthesis to Biomedical Applications: 1-29.
Kim, S., T. Gim and S. M. Kang (2014). "Stability-enhanced polydopamine coatings on solid substrates by iron (III) coordination." Progress in Organic Coatings **77**(8): 1336-1339.
Knott, A., H. Mielke, U. Koop, R. Wolber, T. Burkhardt, J.-P. Vietzke, F. Stäb, H. Wenck and S. Gallinat (2007). "Folic acid: cellular uptake and penetration into human skin." The Journal of Investigative Dermatology **127**(10): 2463-2466.
Kolimi, P., S. Narala and D. Nyavanandi (2022). Innovative treatment strategies to accelerate wound healing: Trajectory and recent advancements. Cells; 11 (15): 1–46.
Li, X.-Q., J.-W. Li, Q.-H. Li, Y. Yan, J.-L. Duan, Y.-N. Cui, Z.-B. Su, Q. Luo, J.-R. Xu and D. YF (2019). "Spectrometric analyses of larotaxel and larotaxel liposomes quantification by high performance liquid chromatography." Beijing da xue xue bao. Yi xue ban= Journal of Peking University. Health Sciences **51**(3): 467-476.
Lin, E., S. E. Calvano and S. F. Lowry (2000). "Inflammatory cytokines and cell response in surgery." Surgery **127**(2): 117-126.
Liu, Y. S., T. S. Li, C. K. Sun, K. C. Wei and C. J. Liu (2016). "The application of phenytoin in the treatment of diabetic ulcers." International Wound Journal **13**(5): 1077.
Lorenz, H. P. and M. T. Longaker (2008). Wounds: biology, pathology, and management. Surgery: basic science and clinical evidence, Springer**:** 191-208.
Luo, G., Z. Li, M. Chen, J. Zheng, X. Deng, G. Xu, M. Cheng, X. Li and Y. Duo (2022). "Three-staged tumor inhibition by mitochondria-targeted cascaded gas/mild-photothermal/photodynamic synergistic therapy." Chemical Engineering Journal **442**: 136169.
Lynge, M. E., P. Schattling and B. Städler (2015). "Recent developments in poly (dopamine)-based coatings for biomedical applications." Nanomedicine **10**(17): 2725-2742.
Man, E. and C. Hoskins (2020). "Towards advanced wound regeneration." European Journal of Pharmaceutical Sciences **149**: 105360.
Mani, G., S. Kim and K. Kim (2018). "Development of folate-thioglycolate-gold nanoconjugates by using citric acid-peg branched polymer for inhibition of MCF-7 cancer cell proliferation." Biomacromolecules **19**(8): 3257-3267.
Mansoori, G. A., K. S. Brandenburg and A. Shakeri-Zadeh (2010). "A comparative study of two folate-conjugated gold nanoparticles for cancer nanotechnology applications." Cancers **2**(4): 1911-1928.

Minogue, A. M., J. P. Barrett and M. A. Lynch (2012). "LPS-induced release of IL-6 from glia modulates production of IL-1β in a JAK2-dependent manner." Journal of neuroinflammation **9**(1): 1-10.
Mirza, R. E., M. M. Fang, W. J. Ennis and T. J. Koh (2013). "Blocking interleukin-1β induces a healing-associated wound macrophage phenotype and improves healing in type 2 diabetes." Diabetes **62**(7): 2579-2587.
Mirza, R. E., M. M. Fang, W. J. Ennis and T. J. J. D. Koh (2013). "Blocking interleukin-1β induces a healing-associated wound macrophage phenotype and improves healing in type 2 diabetes." **62**(7): 2579-2587.
Naderi, N., D. Karponis, A. Mosahebi and A. M. Seifalian (2018). "Nanoparticles in wound healing; from hope to promise, from promise to routine." Frontiers in Bioscience-Landmark **23**(6): 1038-1059.
Nosenko, M., S. Ambaryan and M. Drutskaya (2019). "Proinflammatory cytokines and skin wound healing in mice." Molecular Biology **53**: 653-664.
Palladino, P., F. Bettazzi and S. Scarano (2019). "Polydopamine: surface coating, molecular imprinting, and electrochemistry—successful applications and future perspectives in (bio) analysis." Analytical and bioanalytical chemistry **411**: 4327-4338.
Parvathaneni, V., S. K. Shukla and V. Gupta (2023). "Development and Characterization of Folic Acid-Conjugated Amodiaquine-Loaded Nanoparticles–Efficacy in Cancer Treatment." Pharmaceutics **15**(3): 1001.
Percival, S. L., S. McCarty, J. A. Hunt and E. J. Woods (2014). "The effects of pH on wound healing, biofilms, and antimicrobial efficacy." Wound repair and regeneration **22**(2): 174-186.
Peterson, M. B., S. P. Le-Masurier, K. Lim, J. M. Hook, P. Martens and A. M. Granville (2014). "Incorporation of 5-Hydroxyindazole into the Self-Polymerization of Dopamine for Novel Polymer Synthesis." Macromolecular rapid communications **35**(3): 291-297.
Putra, A., S. Ibrahim, A. M. Muhar, N. Kuntardjo, B. T. Dirja, Z. Pasongka and I. S. Tunru (2022). "Topical gel of mesenchymal stem cells-conditioned medium under TNF-α precondition accelerates wound closure healing in full-thickness skin defect animal model." Journal of Medicine and Life **15**(2): 214.
Ritsu, M., K. Kawakami, E. Kanno, H. Tanno, K. Ishii, Y. Imai, R. Maruyama and M. Tachi (2017). "Critical role of tumor necrosis factor-α in the early process of wound healing in skin." Journal of Dermatology & Dermatologic Surgery **21**(1): 14-19.
Roces, C. B., G. Lou, N. Jain, S. Abraham, A. Thomas, G. W. Halbert and Y. Perrie (2020). "Manufacturing considerations for the development of lipid nanoparticles using microfluidics." Pharmaceutics **12**(11): 1095.
Roces, C. B., E. C. Port, N. N. Daskalakis, J. A. Watts, J. W. Aylott, G. W. Halbert and Y. Perrie (2020). "Rapid scale-up and production of active-loaded PEGylated liposomes." International Journal of Pharmaceutics **586**: 119566.
Rohner, N. A., D. Nguyen and H. A. J. P. von Recum (2020). "Affinity effects on the release of non-conventional antifibrotics from polymer depots." **12**(3): 275.
Ryu, J. H., P. B. Messersmith and H. Lee (2018). "Polydopamine surface chemistry: a decade of discovery." ACS applied materials & interfaces **10**(9): 7523-7540.
Saarinen-Savolainen, P., T. Järvinen, H. Taipale and A. J. I. j. o. p. Urtti (1997). "Method for evaluating drug release from liposomes in sink conditions." **159**(1): 27-33.
Sam, S., L. Touahir, J. Salvador Andresa, P. Allongue, J.-N. Chazalviel, A. Gouget-Laemmel, C. Henry de Villeneuve, A. Moraillon, F. Ozanam and N. Gabouze (2010). "Semiquantitative study of the EDC/NHS activation of acid terminal groups at modified porous silicon surfaces." Langmuir **26**(2): 809-814.
Sayar, H., N. Gergerlioglu, N. Seringec, P. Ozturk, E. Bulbuloglu and G. Karabay (2014). "Comparison of efficacy of topical phenytoin with hypericin in second-degree burn wound healing: an experimental study in rats." Medical science monitor basic research **20**: 36.
Sen, C. K. (2021). "Human wound and its burden: updated 2020 compendium of estimates." Advances in wound care **10**(5): 281-292.
Shalini Devi, K., S. Jacob and A. Senthil Kumar (2018). "In situ structural elucidation and selective Pb2+ ion recognition of polydopamine film formed by controlled electrochemical oxidation of dopamine." Langmuir **34**(24): 7048-7058.

Shini, S., A. Shini and W. L. Bryden (2020). "Unravelling fatty liver haemorrhagic syndrome: 2. Inflammation and pathophysiology." Avian Pathology **49**(2): 131-143.
Sidaway, P. (2015). "Epigenetic changes lead to impaired wound healing in patients with T2DM." Nature Reviews Endocrinology **11**(2): 65-65.
Simón, M. (2016). "Active leptospermum honey: a strategy to prevent chronic wounds." The Journal for Nurse Practitioners **12**(5): 339-345.
Soleymani, J., S. Azizi, S. Abbaspour-Ravasjani, M. Hasanzadeh, M. H. Somi and A. Jouyban (2021). "Glycoprotein-based bioimaging of HeLa cancer cells by folate receptor and folate decorated graphene quantum dots." Microchemical Journal **170**: 106732.
Song, J.-M., J.-H. Im, J.-H. Kang and D.-J. Kang (2009). "A simple method for hyaluronic acid quantification in culture broth." Carbohydrate polymers **78**(3): 633-634.
Suarez-Arnedo, A., F. T. Figueroa, C. Clavijo, P. Arbeláez, J. C. Cruz and C. Muñoz-Camargo (2020). "An image J plugin for the high throughput image analysis of in vitro scratch wound healing assays." PloS one **15**(7): e0232565.
Sun, Y. and E. W. Davis (2022). "Multi-Stimuli-Responsive Janus Hollow Polydopamine Nanotubes." Langmuir **38**(32): 9777-9789.
Sunoqrot, S., J. W. Bae, S.-E. Jin, R. M. Pearson, Y. Liu and S. Hong (2011). "Kinetically controlled cellular interactions of polymer− polymer and polymer− liposome nanohybrid systems." Bioconjugate chemistry **22**(3): 466-474.
Walter, M. N., K. T. Wright, H. R. Fuller, S. MacNeil and W. E. B. Johnson (2010). "Mesenchymal stem cell-conditioned medium accelerates skin wound healing: an in vitro study of fibroblast and keratinocyte scratch assays." Experimental cell research **316**(7): 1271-1281.
Wang, X., S. Zhang, M. Dong, Y. Li, Q. Zhou and L. Yang (2020). "The proinflammatory cytokines IL-1β and TNF-α modulate corneal epithelial wound healing through p16Ink4a suppressing STAT3 activity." Journal of Cellular Physiology **235**(12): 10081-10093.
Wang, Y., W. Zhang, Q. Lv, J. Zhang and D. Zhu (2016). "The critical role of quercetin in autophagy and apoptosis in HeLa cells." Tumor Biology **37**: 925-929.
Wu, I. Y., S. Bala, N. Škalko-Basnet and M. P. Di Cagno (2019). "Interpreting non-linear drug diffusion data: Utilizing Korsmeyer-Peppas model to study drug release from liposomes." European Journal of Pharmaceutical Sciences **138**: 105026.
Yang, H., L. Song, Y. Zou, D. Sun, L. Wang, Z. Yu and J. Guo (2020). "Role of hyaluronic acids and potential as regenerative biomaterials in wound healing." ACS Applied Bio Materials **4**(1): 311-324.
Yang, W., C. Liu and Y. Chen (2018). "Stability of polydopamine coatings on gold substrates inspected by surface plasmon resonance imaging." Langmuir **34**(12): 3565-3571.
Yoshitomi, R., K. Nakayama, S. Yamashita, M. Kumazoe, T.-A. Lin, C.-Y. Mei, Y. Marugame, Y. Fujimura, M. Maeda-Yamamoto and S. Kuriyama (2020). "Plasma homocysteine concentration is associated with the expression level of folate receptor 3." Scientific reports **10**(1): 10283.
Yu, F., S. Chen, Y. Chen, H. Li, L. Yang, Y. Chen and Y. Yin (2010). "Experimental and theoretical analysis of polymerization reaction process on the polydopamine membranes and its corrosion protection properties for 304 Stainless Steel." Journal of Molecular Structure **982**(1-3): 152-161.
Zhang, P., Q. Xu, X. Li and Y. Wang (2020). "pH-responsive polydopamine nanoparticles for photothermally promoted gene delivery." Materials Science and Engineering: C **108**: 110396.